ELSEVIER

Journal of Fluids and Structures 26 (2010) 482–502

JOURNAL OF FLUIDS AND STRUCTURES

www.elsevier.com/locate/jfs

Three-dimensional numerical simulations of cross-flow around four cylinders in an in-line square configuration

K. Lam[a,*], L. Zou[b]

[a]*Department of Mechanical Engineering, The Hong Kong Polytechnic University, Hung Hom, Kowloon, Hong Kong*
[b]*School of Mechanical and Electronic Engineering, Wuhan University of Technology, Wuhan 430070, China*

Received 30 September 2008; accepted 30 December 2009
Available online 12 February 2010

Abstract

This paper presents a numerical study of three-dimensional (3-D) laminar flow around four circular cylinders in an in-line square configuration. The investigation focuses on effects of spacing ratio (L/D) and aspect ratio (H/D) on 3-D flow characteristics, and the force and pressure coefficients of the cylinders. Extensive 3-D numerical simulations were performed at Reynolds number of 200 for L/D from 1.6 to 5.0 at $H/D = 16$ and H/D from 6 to 20 at $L/D = 3.5$. The results show that the 3-D numerical simulations have remedied the inadequacy of 2-D simulations and the results are in excellent agreement with the experimental results. The relation between 3-D flow patterns and pressure characteristics around the four cylinders is examined and discussed. The critical spacing ratio for flow pattern transformation was found to be $L/D = 3.5$ for $H/D = 16$, while a bistable wake pattern was observed at $L/D = 1.6$ for the same aspect ratio. Moreover, a transformation of flow pattern from a stable shielding flow pattern to a vortex shedding flow pattern near the middle spanwise positions of the cylinders was observed and was found to be dependent on the aspect ratio, spacing ratio, and end wall conditions. Due to the highly 3-D nature of the flows, different flow patterns coexist over different spanwise positions of the cylinders even for the same aspect ratio. It is concluded that spacing ratio, aspect ratio, and the no-slip end wall condition have important combined effects on free shear layer development of the cylinders and hence have significant effects on the pressure field and force characteristics of the four cylinders with different spacing ratios and aspect ratios.

Keywords: Three-dimensional; Simulations; Four cylinders; Aspect ratio; Spacing ratio

1. Introduction

Flow past cylinder arrays can be found in many engineering applications, such as heat exchangers, offshore structures, and even micro-electro-mechanical systems. The complexity of flow separation and free shear layer interference generated by the cylinder arrays has attracted considerable attention in the past. For example, Moulinec et al. (2004) numerically investigated flow past a staggered array of rigid cylinders with two different spacing ratios at Reynolds numbers from 50 to 6000. Kevlahan (2007) investigated the stability of the periodic wake of tightly packed rotated and in-line infinite cylinder arrays in laminar flow conditions. In general, the complex flow pattern is due to

*Corresponding author. Tel.: +852 2766 6649; fax: +852 2365 4703.
E-mail address: mmklam@polyu.edu.hk (K. Lam).

0889-9746/$ - see front matter © 2010 Elsevier Ltd. All rights reserved.
doi:10.1016/j.jfluidstructs.2010.01.001

different flow conditions, such as variation of cylinder spacing ratio L/D (L is the centre-to-centre spacing between the upstream and downstream cylinders and D the diameter of the cylinder), aspect ratio H/D (H is the spanwise height of the cylinder), end conditions, blockage ratio, the Reynolds number, etc.

Over the past years, numerous studies on flow around four-cylinder arrays have been carried out using experimental and numerical techniques. Sayers (1988, 1990) conducted experiments on four cylinders in a square configuration at Reynolds number of 30 000. Lam and Lo (1992) and Lam et al. (2003a) carried out visualization studies to understand effects of the spacing ratio on flow patterns and vortex shedding frequency. Lam and Fang (1995) and Lam et al. (2003b) measured the pressure distributions and the lift/drag coefficients on four cylinders with the spacing ratio varying from 1.26 to 5.8. Lam and Zou (2007) further investigated effects of the spacing ratio and Reynolds number on mean velocity distribution and flow patterns around the four in-line cylinders at subcritical Reynolds numbers using laser Doppler anemometer (LDA) and digital particle image velocimetry (DPIV) techniques. Farrant et al. (2000) captured two-dimensional (2-D) flow characteristics and interactive forces associated with flow around four equispaced cylinders for two orientations (in-line arrangement and an alignment angle of 45° arrangement) for spacing ratios $L/D = 3$ and 5 at $\mathrm{Re} = 200$ using a cell boundary element method. With the typical case of four cylinders being arranged with alignment angle of 45° and the case of in-line arrangement at $L/D = 5$, the computation results showed agreement with visualization results obtained by Lam and Lo (1992) and Lam et al. (2003a, b). However, it is interesting to note that for the in-line arrangement with $L/D = 3$, the computational results showed that shear layers from upstream cylinders roll up into mature vortices and impinge on the downstream cylinders' surface. This result is different from that obtained using flow visualization, which showed a shielding flow pattern behind the upstream cylinders. Lam and Lo (1992) suggested that the distinct vortex shedding of the upstream cylinders was suppressed below $L/D = 3.94$ in the in-line arrangement. Lam et al. (2003a) reconfirmed that accurate prediction of the shielding flow pattern for the critical arrangement is a challenge for numerical simulation. Moreover, Lam et al. (2008) performed 2-D simulations on four-cylinder arrays with different spacing ratios at low Reynolds numbers of 100 and 200 using the finite volume method. They failed to simulate the shielding flow pattern for the same arrangement. This indicates that there is a large discrepancy between experimental measurements and computational results at the critical spacing ratios. It should be noted that all of the numerical simulations above were carried out by assuming 2-D flow around the four cylinders, in spite of the actual 3-D flow around them. For an adequate representation of flow around four cylinders, a relatively time-consuming 3-D simulation should be carried out. Lam and Zou (2007) employed 3-D large eddy simulation on turbulent cross-flow around four in-line cylinders with different spacing ratios at a subcritical Reynolds number. The numerical results predict accurately some of the wake flow characteristics around four cylinders and agree with the experimental measurements. However, more extensive investigations about 3-D vortex structures and the effect of space ratio and aspect ratio on the cylinder arrays have yet to be carried out.

Apart from studies on flow around four-cylinder arrays, experimental and numerical studies on 3-D flows past one or two cylinders have been extensively investigated. These findings indicated that the aspect ratio has strong effects on the force and pressure characteristics and the wake development behind the cylinder. For example, Luo et al. (1996) measured experimentally the pressure distribution on two finite tandem cylinders. Analyzing the surface pressure distributions at different parts of the cylinder span, they pointed out that the flow patterns change as H/D increases but the change no longer takes place over the entire span simultaneously due to the 3-D nature of the flow. Okamoto and Sunabashiri (1992) investigated a finite length cylinder of aspect ratio H/D of 0.5–23.75 and reported that the drag coefficient of the cylinder increased with increasing H/D. Szepessy and Bearman (1992) measured in detail the fluctuating forces and shedding frequency on a circular cylinder at the aspect ratios of 0.25–12 and found that the aspect ratio has the most striking effect on the fluctuating lift. Norberg (1994) extensively studied the effect of the aspect ratio for the mean base suction coefficient and shedding frequency on a circular cylinder of various aspect ratios in laminar shedding, transitional and turbulent flows. Parallel shedding at around the mid-span was observed throughout the laminar shedding regime in some cases. At smaller aspect ratios H/D, the negative base pressure coefficient decreases with decreasing H/D. Mittal (2001) presented a 3-D finite element simulation for unsteady flow past cylinders of low aspect ratios and confirmed that the end conditions for the finite cylinder determine the mode of vortex shedding. Moreover, So et al. (2005) carried out numerical simulations for a rigid slender cylinder at aspect ratio $6 \leq H/D \leq 16$ to examine 3-D wake effects on the flow-induced forces using the finite volume method and lattice Boltzmann method. They pointed out that the aspect ratio has a significant effect on the 3-D flow wake and the flow-induced force.

Considering investigations on the cross-flow past four-cylinder arrays, most of the previous studies are focused on effects of the spacing ratio. The effects of the aspect ratio of four-cylinder arrays together with end wall conditions have not yet been fully investigated. The understanding of the complex physical mechanism of 3-D flow characteristics around four cylinders in the in-line square configuration (especially effects of the spacing ratio and aspect ratio on flow characteristics of four cylinders) is still lacking. The present research performs extensive 3-D numerical simulations on laminar flow around four cylinders in an in-line square configuration, using a finite volume method, in order to obtain

time-dependent quantitative information, which is very difficult to obtain by experimental measurements. Flow visualization was carried out in a water tunnel by employing the LIF technique, mainly to validate and supplement the present 3-D numerical simulations. The main objectives of the present work are to investigate the combined effects of spacing ratio and aspect ratio on the 3-D vortex structures, the Strouhal number, and force and pressure coefficient distributions for flow around four circular cylinders in the in-line square configuration at laminar flow condition with Re = 200. The discrepancy between experimental observations and numerical results is clarified. It is hoped that the study provides deeper understanding on the physical processes of 3-D free shear layer development and vortex formation around four cylinders in an in-line square configuration for various spacing ratios and aspect ratios.

2. Numerical methods

2.1. Governing equations

The dimensionless 3-D Navier–Stokes equations governing the flow of a Newtonian fluid can be written in vector form as

$$\frac{\partial \mathbf{u}}{\partial t} + \mathbf{u} \cdot \nabla \mathbf{u} = -\nabla p + \frac{1}{\mathrm{Re}} \nabla^2 \mathbf{u}, \tag{1}$$

$$\nabla \cdot \mathbf{u} = 0, \tag{2}$$

where $\mathrm{Re} = U_\infty D/v$ is the Reynolds number, U_∞ being the oncoming free-stream velocity, v is the fluid kinematic viscosity, and D is the diameter of the cylinder.

In the present simulations, the Reynolds number is kept at Re = 200. The nondimensional velocity vector $\mathbf{u}$ in the Cartesian coordinates (x, y, z) has three velocity components u, v, and w, respectively, and p is the nondimensional static pressure. In solving the governing equations, the different physical quantities are normalized by the free-stream velocity and the diameter of the cylinder. The finite volume method is applied on unstructured hexahedral meshes. The pressure–velocity coupling is handled with the semi-implicit pressure linked equations (SIMPLE) scheme. Discretization of the convective terms in the conservation equations is accomplished through a second-order accurate upwind differencing scheme. Second-order implicit forward discretization is adopted for the time derivative term in order to accelerate the convergence process.

2.2. Computational models and boundary conditions

Fig. 1 shows a schematic diagram of the computational domain for the simulation of flow around four cylinders in an in-line square configuration. The computational models are specified to resemble the "no-slip" wall condition, which corresponds to the experimental study in a water tunnel with flow around these four cylinders with different spacing ratios and aspect ratios. The origin of the coordinate system is located at the center point of the four-cylinder arrangement on the tunnel floor with (x, y, z) denoting the coordinates along the streamwise x-direction, the transverse y-direction, and the cylinder spanwise z-direction, respectively. The computational domain is chosen to be $32D \times 20D \times HD$ with the upstream and downstream boundaries located at $8D$ and $24D$, respectively, from the coordinate origin. The lateral surfaces are located at $10D$ each from the coordinate origin.

At the inlet, a uniform velocity profile ($u = 1$, $v = w = 0$) is imposed. A Neumann-type boundary condition is used at the outlet boundary. No-slip boundary condition ($u = v = w = 0$) is employed on the surfaces of the cylinders. At the lateral surfaces of the computational domain, symmetry boundary conditions are used. In the present simulations, the spacing ratio L/D varies from 1.6 to 5, while the aspect ratio H/D varies from 6 to 20. Only half of the height of the cylinder is simulated in order to save computational time. As shown in Fig. 1 (upper right), the bottom of computational domain is set with the no-slip wall condition while the symmetry boundary condition is imposed at the mid-span plane ($z = H/2$). Mittal (2001) successfully applied this kind of symmetry boundary condition to study the effect of the "no-slip" wall on a finite single cylinder at Reynolds numbers from 100 to 1000. Lam et al. (2008) also adopted such a symmetry boundary condition to simulate cross-flow past a 3-D cylinder array at an aspect ratio of $16D$.

2.3. Validation of the numerical method and grid independence test

In order to confirm the suitability of the symmetry boundary condition at the mid-span plane adopted for the present numerical models, "no-slip" wall boundary conditions at both ends and periodic boundary conditions at both ends of

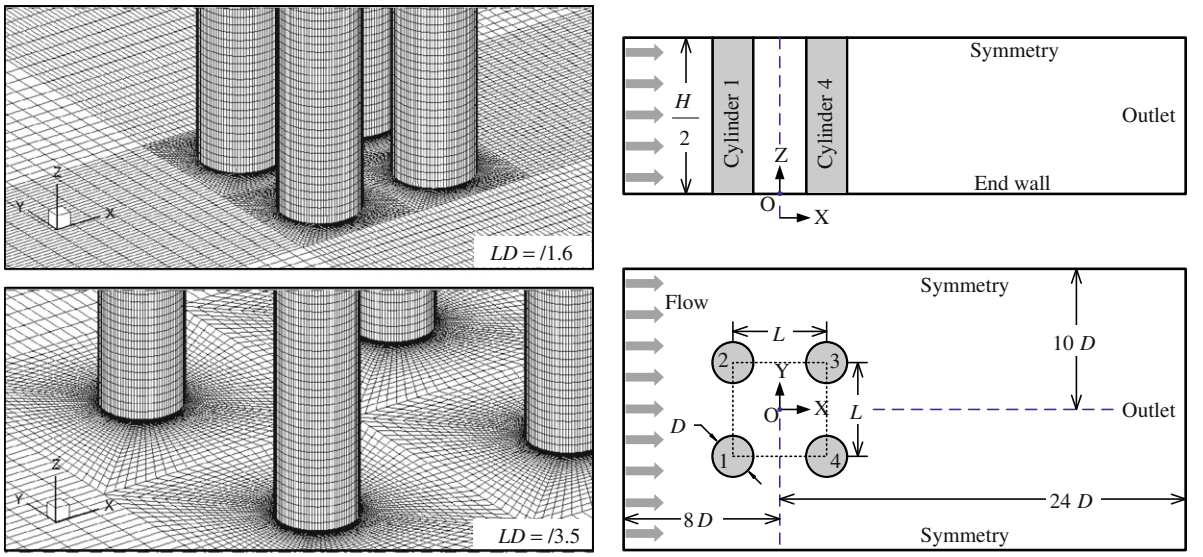

Fig. 1. Grid distributions around the four cylinders with different configurations and schematics of the computational domains.

Table 1
Comparison of $\overline{C}_D$, C'_L, and St with different boundary conditions at $H/D = 8$, $L/D = 3.5$, and $Re = 200$.

H/D	Boundary condition	$\overline{C}_{D1}$	$\overline{C}_{D2}$	$\overline{C}_{D3}$	$\overline{C}_{D4}$	C'_{L1}	C'_{L2}	C'_{L3}	C'_{L4}	St_3	St_4
8	Symmetry	1.334	1.334	0.327	0.327	0.005	0.005	0.236	0.236	0.151	0.151
16	No-slip wall	1.335	1.335	0.324	0.324	0.009	0.009	0.277	0.277	0.152	0.152
8	Periodic	1.372	1.372	0.978	0.978	0.618	0.618	1.414	1.414	0.195	0.195

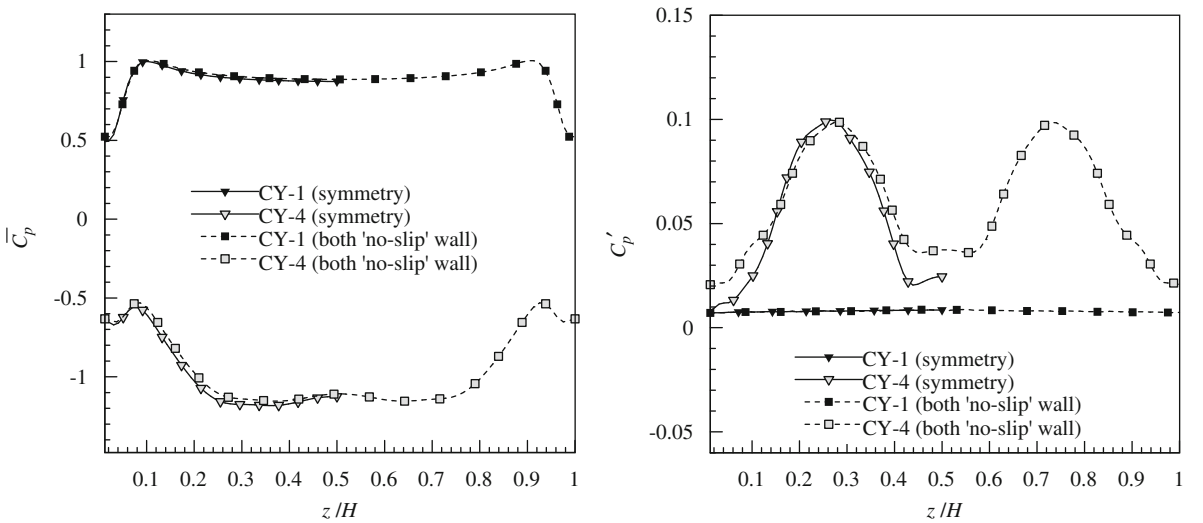

Fig. 2. Variation of the mean pressure coefficient and fluctuating pressure coefficient along the spanwise direction of the cylinders employing two different boundary conditions at x–z plane ($\theta = 0^\circ$) for $L/D = 3.5$ and $H/D = 16$.

the cylinders were also utilized for comparison at $L/D = 3.5$ and $H/D = 8$. Table 1 shows the calculated values of mean drag coefficient ($\overline{C}_D = 2\overline{F}_D/\rho U_\infty^2 DH$), the root-mean-square (r.m.s.) fluctuating lift coefficient ($C_L' = 2F_L'/\rho U_\infty^2 DH$), and the Strouhal number ($St = f_s D/U_\infty$) with different boundary conditions. Here, $\overline{F}_D$ is the total mean drag force, F'_L the r.m.s. lift force, and f_s the vortex shedding frequency obtained by fast Fourier transform (FFT) of the time history of the fluctuating lift. The computational results of $\overline{C}_D$, C'_L, and St employing the symmetry boundary condition show good agreement with those of the "no-slip" boundary conditions at two walls. The difference of $\overline{C}_D$ and St obtained by the two boundary conditions is less than 1%. When employing periodic boundary conditions, some of the computational results are in line with the 2-D results obtained by Farrant et al. (2000) and Lam et al. (2008). This is because periodic boundary conditions in 3-D simulations are analogous to 2-D simulations, where the cylinders are assumed to be infinitely long. However, there are large discrepancies between the values of $\overline{C}_D$, C'_L, and St when adopting periodic boundary conditions and the values of $\overline{C}_D$, C'_L, and St when employing symmetry boundary conditions and "no-slip" wall boundary conditions at both ends of the cylinder. The values of $\overline{C}_D$ and St of the downstream cylinders are 66.5% and 22.4%, respectively, higher than those employing "no-slip" wall boundary conditions. This indicates that the effect of end wall condition should not be ignored. Fig. 2 shows that variations of mean pressure coefficient ($\overline{C}_p$) and that of mean fluctuating pressure coefficient C'_p, r.m.s. value) along the span of the cylinders at the position $\theta = 0^\circ$ for symmetry boundary conditions and both "no-slip" wall boundary conditions are in good agreement with each other. The values of $\overline{C}_p$ and C'_p exhibited a fairly symmetrical distribution about the mid-span plane along the cylinders for both "no-slip" wall boundary conditions. Therefore, the symmetry boundary conditions employed in the present study are justifiable.

Furthermore, grid independence test for the flow around a single cylinder ($H/D = 16$) was carried out before the extensive simulations. The computational domain size is defined similar to that of the four-cylinder cases. There are five meshing schemes being tested. The numbers of grids employed are 80, 100, and 160 around the circumference of the cylinder corresponding to cell numbers of 9100, 11 000, and 16 400, respectively, in x–y plane. There are correspondingly 64, 80, and 128 grids in the spanwise z-direction, respectively. The dimensionless time step (tU_∞/D) is set to 0.02. The first level of the grid spacing in the radial direction close to the cylinder surface and the end wall is $0.005D$ for adequate resolution of the boundary layer and then increases with an expansion rate of 1.1 in the radial direction. Table 2 shows the comparison of $\overline{C}_D$, C'_L, and St of the present numerical results with previous experimental and numerical results of a single cylinder at $Re = 200$. It can be seen that the difference of $\overline{C}_D$, C'_L, and St between the present cases with different meshing schemes is less than 4%, 6%, and 1%, respectively, except for present cases 1 and 2. Moreover, the values of $\overline{C}_D$ and St employing these meshing schemes are generally in good agreement with the previous experimental and computational results, with the exception of the 2-D results of $\overline{C}_D$ by Chan and Anastasiou (1999) and the 3-D result of St computed with periodic boundary conditions at the ends of the cylinder by Zhang and Dalton (1998). However, the present results for C'_L for a single cylinder show a large difference with previous results by Zhang and Dalton (1998). The differences may be due to different simulation conditions by the different authors. Norberg (2003) made an extensive review of previous experimental and numerical investigations concerning fluctuating lift acting on a single cylinder. The value of C'_L was summarized to be within the range 0.15–0.65. The present simulation results were found to be also within this range. Therefore, the accuracy of the present simulation results is considered to be acceptable. Table 3 shows the grid independence test for a four-cylinder model with $H/D = 16$ and $L/D = 3.5$ at

Table 2
Grid independence test and numerical method validation for a single circular cylinder at $Re = 200$.

Case		H/D	Grid	$\overline{C}_D$	C'_L	St
Zhang and Dalton (1998)	3-D	15	–	1.32	0.43	0.198
Persillon and Braza (1998)	3-D	20	–	1.31	0.254	0.181
Chan and Anastasiou (1999)	2-D		–	1.48	–	0.180
Carmo and Meneghini (2006)	3-D	12	–	1.28	–	0.184
Williamson (1996)	Exp.	–	–	–	–	0.183
Fey et al. (1998)	Exp.	–	–	–	–	0.183
Norberg (2003)		–	–	–	0.15–0.65	0.175–0.196
Present case 1	3-D	16	9100×80	1.26	0.186	0.180
Present case 2	3-D	16	$11\,000 \times 64$	1.23	0.174	0.178
Present case 3	3-D	16	$11\,000 \times 80$	1.29	0.227	0.182
Present case 4	3-D	16	$11\,000 \times 128$	1.30	0.241	0.180
Present case 5	3-D	16	$16\,400 \times 80$	1.27	0.233	0.181

Table 3
Grid independence test for a four-cylinder model ($H/D = 16$, $L/D = 3.5$) at Re = 200.

Case	$Lx \times Ly \times Lz$ (D)	Grid	$\overline{C}_{D1}$	$\overline{C}_{D4}$	C'_{L1}	C'_{L4}	St_4
Case 1	$32 \times 20 \times 8$	$13\,200 \times 80$	1.291	0.473	0.059	0.431	0.159
Case 2	$32 \times 20 \times 8$	$18\,700 \times 80$	1.314	0.481	0.064	0.446	0.160
Case 3	$32 \times 20 \times 8$	$18\,700 \times 160$	1.321	0.487	0.062	0.440	0.161
Case 4	$32 \times 20 \times 8$	$25\,300 \times 80$	1.319	0.484	0.065	0.451	0.160

Table 4
Computational models for the cross-flow around four cylinders in an in-line square configuration.

Models	L/D	H/D	$Lx \times Ly \times Lz$ (D)	Grid
Case A	1.6	16	$32 \times 20 \times 8$	$18\,500 \times 80$
Case B	2.5	16	$32 \times 20 \times 8$	$18\,700 \times 80$
Case C	3.0	16	$32 \times 20 \times 8$	$18\,700 \times 80$
Case D_1	3.5	6	$32 \times 20 \times 3$	$18\,700 \times 32$
Case D_2		8	$32 \times 20 \times 4$	$18\,700 \times 48$
Case D_3		12	$32 \times 20 \times 6$	$18\,700 \times 64$
Case D_4		14	$32 \times 20 \times 7$	$18\,700 \times 70$
Case D_5		15	$32 \times 20 \times 7.5$	$18\,700 \times 76$
Case D_6		16	$32 \times 20 \times 8$	$18\,700 \times 80$
Case D_7		20	$32 \times 20 \times 10$	$18\,700 \times 100$
Case D_8		8 (periodic)	$32 \times 20 \times 8$	$18\,700 \times 80$
Case E	4.0	16	$32 \times 20 \times 8$	$19\,200 \times 80$
Case F	5.0	16	$32 \times 20 \times 8$	$20\,540 \times 80$

Re = 200. The numbers of grids employed are 80, 100, and 160 around the circumference of the cylinder corresponding to cell numbers of 13 200, 18 700, and 25 300, respectively, in x–y plane. Moreover, in the spanwise z-direction, grid layers of 80 and 160 are chosen. All the grid independence tests show that the present grid schemes are applicable for the present study.

Considering the accuracy and cost of computation, the meshing scheme with the grid number of 100 around the circumferential direction is chosen for the present four-cylinder simulations. This will give cell numbers of 18 500–20 540 in the x–y plane for spacing ratios (L/D) varied from 1.6 to 5. The grid layers along the spanwise direction were varied from 32 to 100 when the aspect ratios (H/D) varied from 6 to 20. For all of the present simulations, at least 300 dimensionless time steps, which correspond to about 60 vortex shedding cycles, were taken so as to obtain more reliable statistical information.

3. Results and discussion

Table 4 lists all of the computational models for simulating flow around four-cylinder arrays with different spacing ratios and aspect ratios. Referring to the previous investigations on the spacing ratio effect, the present 3-D simulations were carried out with the spacing ratios of $1.6 \leq L/D \leq 5$ at the aspect ratio of $H/D = 16$ [refer to the previous studies on a single cylinder with a finite length by Mittal (2001) and So et al. (2005)]. Moreover, 3-D simulations at the aspect ratios of $6 \leq H/D \leq 20$ and the critical spacing ratio $L/D = 3.5$ [refer to the previous results by Lam et al. (1992–2008)] have been carried out. An example employing the periodic boundary condition with $H/D = 8$ is also included to enhance our understanding on the significance of aspect ratio and end condition.

3.1. Effect of L/D and H/D on force characteristics and Strouhal numbers

The previous investigations by Lam and Lo (1992), Lam and Fang (1995), Lam et al. (2003a), and Sayers (1988, 1990) showed that the flow around four cylinders in the in-line square configuration can be regarded as a mirror image of two

parallel rows of two-cylinder arrays in tandem. The wake interference from the side-by-side cylinders exhibits approximately symmetrical phenomena about the centreline of four cylinders except at small spacing ratios $L/D \leq 2.0$. In general, the force coefficients and vortex shedding frequencies of both the upstream cylinders 1 and 2 as well as those of the downstream cylinders 3 and 4 are similar to each other. This leads to the following discussion of the flow characteristics on cylinders 1 and 4.

Figs. 3(a) and (b) show the values of $\overline{C}_D$ and C'_L for the cylinders 1 and 4 with different spacing ratios ($1.6 \leq L/D \leq 5$) and a fixed aspect ratio of $H/D = 16$ at $\mathrm{Re} = 200$. All values are time-averaged results over the entire span of the cylinders. The value of $\overline{C}_D$ for the upstream cylinder 1 decreases slightly until $L/D = 3.5$ and then increases again while the value of $\overline{C}_D$ for the downstream cylinder 4 increases with increasing L/D. The value of C'_L for both upstream cylinder 1 and downstream cylinder 4 increases gradually as L/D increases. Such a trend is in good agreement with the experimental results by Lam et al. (2003b) at subcritical Reynolds number. It is also interesting to note that, in the present simulation for $L/D = 1.6$, the values of $\overline{C}_D$ and C'_L of the downstream cylinder 3 are different from those of the downstream cylinder 4 by 1.75 times and 1.3 times, respectively. This is attributed to the bistable shielding flow pattern characteristics. The results of $\overline{C}_D$ and C'_L for 2-D simulations of flow around four cylinders by Lam et al. (2008) are also included for comparison. The 2-D results show evident discrepancies with the present 3-D results and the experimental measurements by Lam et al. (2003b), especially for the values of C'_L. Different values of $\overline{C}_D$ occur at the spacing ratios of $L/D \geq 4$, while different values of C'_L occur at $L/D \geq 3.5$. This implies that the critical spacing ratio is

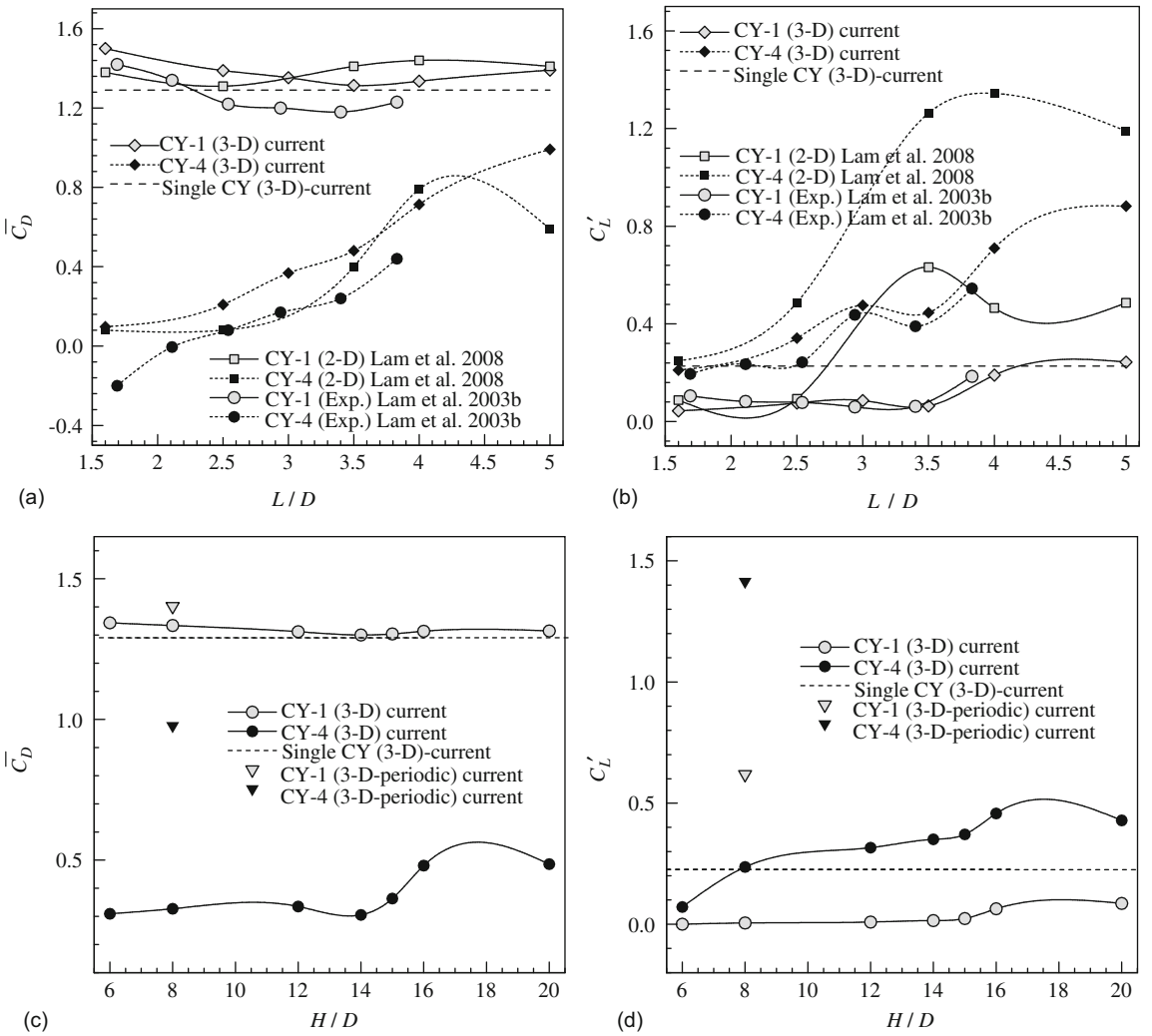

Fig. 3. Mean drag coefficients and fluctuating lift coefficients: (a, b) with different spacing ratios L/D at $H/D = 16$ and (c, d) with different aspect ratios H/D at $L/D = 3.5$.

within the range $3.5 \le L/D \le 4$ and it has a strong 3-D effect on the wake structures, which cannot be captured by 2-D simulations. The vortex shedding frequencies of the four cylinders are plotted in Fig. 4(a) for different spacing ratios. For spacing ratios of $1.6 \le L/D \le 3.5$, the Strouhal number for cylinder 4 is slightly lower than that of a single cylinder, while it becomes slightly larger when $L/D > 4$. In general, the value of St of the downstream cylinder 4 is close to that of a single cylinder (St = 0.18). For upstream cylinder 1, however, no vortex shedding occurs until $L/D > 3.5$. This further confirms that the critical spacing ratio is in the range $3.5 \le L/D \le 4$.

Figs. 3(c) and (d) show the variations of $\overline{C}_D$ and C'_L with aspect ratios $6 \le H/D \le 20$ at spacing ratio $L/D = 3.5$. For all aspect ratios, $\overline{C}_D$ of upstream cylinder 1 is quite similar to that of a single cylinder and it is slightly lower than the simulation value using periodic boundary conditions. The aspect ratio does not have a distinct effect on $\overline{C}_D$ of upstream cylinder 1. However, the value of $\overline{C}_D$ of downstream cylinder 4 increases from 0.3 to 0.5 as H/D increases from 6 to 20. It is noted that the $\overline{C}_D$ of downstream cylinder 4 increases by approximately 1.6 times, associated with a sharp increase in C'_L when H/D changes from 14 to 16. This variation in characteristics implies that there is a great change of flow pattern at such an aspect ratio range. This indicates that a critical aspect ratio exists around $H/D = 16$, which has a strong effect on $\overline{C}_D$ and C'_L due to the occurrence of 3-D wake structures. With the variation of aspect ratio, all the

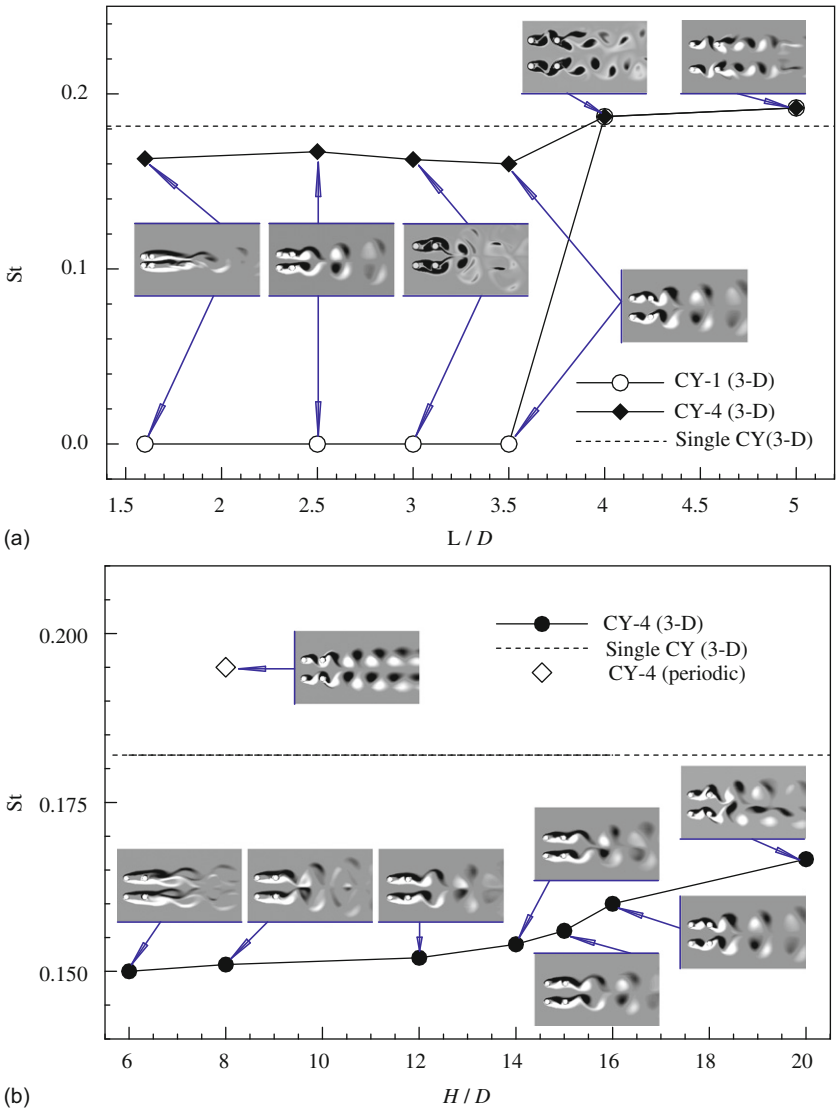

Fig. 4. Strouhal numbers and corresponding flow patterns at mid-plane for cylinders: (a) with different spacing ratios (L/D) compared with a circular cylinder at $H/D = 16$ and (b) with different aspect ratios (H/D) at $L/D = 3.5$.

values of $\overline{C}_D$ of downstream cylinder 4 are less than 50% of the $\overline{C}_D$ of the values for the same cylinder associated with periodic boundary conditions. This implies that the simulations employing periodic boundary conditions have resulted in a significantly different flow pattern compared with that using "no-slip" end wall conditions. This also explains why 2-D simulations cannot replicate the four-cylinder flow field completely. Moreover, for all cylinder cases with the end wall conditions and different aspect ratios, both C'_L of the upstream cylinders and the downstream cylinders are much smaller than those using periodic boundary conditions. Especially at $H/D = 6$, C'_L of the upstream and downstream cylinders are significantly suppressed. This again indicates that the aspect ratio and the end wall condition have a strong combined effect on the fluctuating lift coefficients of the four cylinders. Moreover, the changes of $\overline{C}_D$ and C'_L of downstream cylinder 4 are significantly larger than the changes of $\overline{C}_D$ and C'_L of the upstream cylinder 1 when H/D varies.

The variation of Strouhal number for cylinder 4 with different aspect ratios is plotted in Fig. 4(b). It increases gradually as H/D increases and demonstrates the dependent character on aspect ratio, especially for $H/D \geq 16$. The Strouhal number of the downstream cylinders is about 0.16 at $H/D = 16$, which is close to the experimental value obtained at much higher Reynolds number by Lam et al. (2003b). They found that the St of downstream cylinder 4 is around 0.17 at $H/D = 17$ for $\mathrm{Re} = 4.1 \times 10^4$ for the same configuration.

3.2. Effect of L/D on the 3-D vortex structures

Instantaneous pressure distributions and force characteristics are determined by instantaneous flow patterns and vortex structures around the cylinders. Lam et al. (2008) pointed out that the fluctuating pressure coefficients of the downstream cylinders increase more than 20 times when they are impinged by vortices from the upstream cylinders. Therefore, it is extremely important to obtain a clear picture of the effect of L/D and H/D on the 3-D vortex structures around the cylinders in order to understand pressure and force characteristics of the cylinders. The distributions of spanwise vorticity (ω_z) in the x–y plane for the cylinders at $L/D = 1.6$, 2.5, 3.5, and 5.0 are plotted in Fig. 5. The iso-surfaces of the 3-D vortex structures behind the four cylinders are also captured. Three x–y plane sections at different spanwise locations ($z/H = 0.0625$ (near end wall), 0.125, and 0.25) are selected to illustrate the vorticity behavior

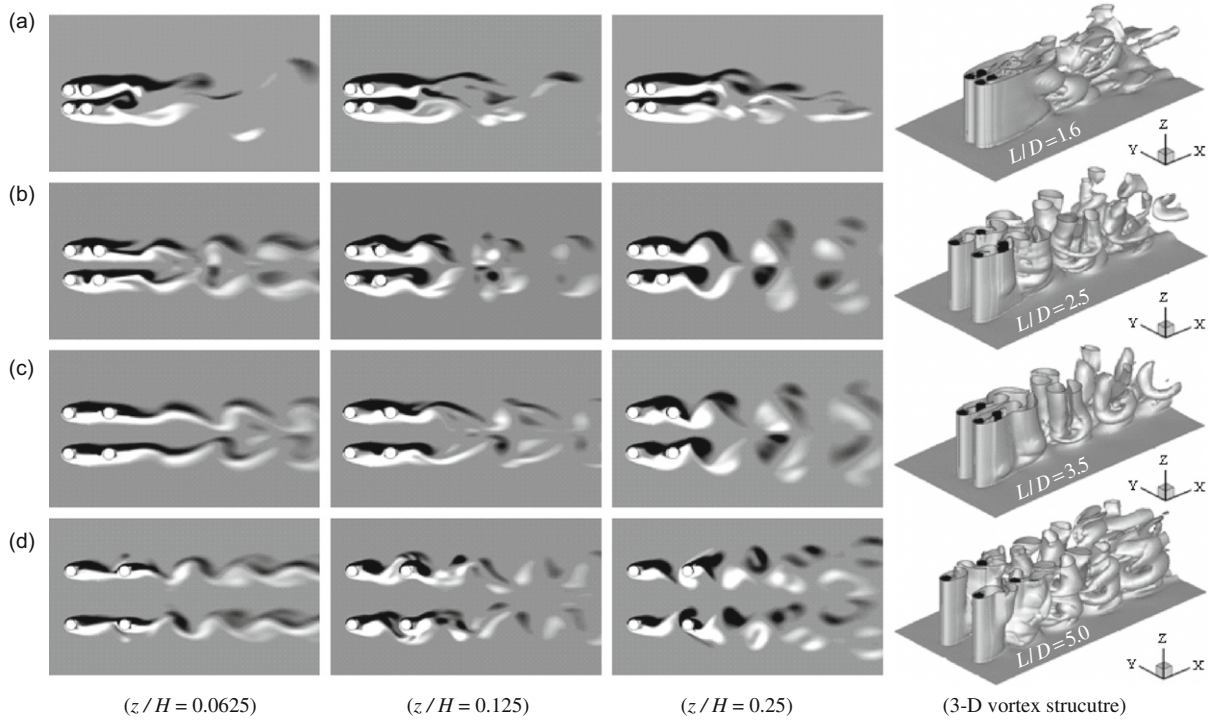

Fig. 5. Flow patterns at the different spanwise positions and 3-D vortex structures for the different spacing ratios with $H/D = 16$: (a) $L/D = 1.6$, (b) $L/D = 2.5$, (c) $L/D = 3.5$, and (d) $L/D = 5.0$.

between the mid-plane and the end wall. The vortex patterns at $z/H = 0.5$ (the mid-plane) are incorporated in Fig. 4(a) for illustration of their effects on vortex shedding characteristics. The vorticity plots clearly show that the flow patterns around the four cylinders for all spacing ratios display a spanwise dependency. The vortex structures at the mid-spans of the cylinders in the present simulations are also fairly consistent with the experimental results obtained by Lam and Lo (1992), and Lam et al. (2003a, b).

Fig. 5(a) shows the flow patterns and 3-D vortex structures of the four cylinders at a small spacing ratio $L/D = 1.6$ with $H/D = 16$. It can be clearly observed that the downstream cylinders are completely shielded by the free shear layers from their corresponding upstream cylinders in all spanwise positions. A bistable behavior evolves behind the downstream cylinders due to the effects of jet-like flow characteristics between the two columns of cylinders. Deflection angles of the biased flow appear to be sensitive to variation in z/H (spanwise location), with an increasing trend from $z/H = 0.0625$ position towards the mid-span of the cylinders. At $z/H = 0.5$ (see Fig. 4(a)), a wide wake with low shedding frequency $St = 0.125$ (cylinder 3) and a narrow wake with high shedding frequency $St = 0.163$ (cylinder 4) are attached to the downstream cylinders, which intermittently switch at different computation time instants. However, this bistable nature of the wake flow is not periodic, but appears to be completely random. Similar experimental results were recorded by Lam and Cheung (1988) and Lam and Lo (1992). Further downstream the instantaneous 3-D vortex structures at $L/D = 1.6$ show non-uniform distribution along the spanwise direction.

For $L/D = 2.5$ (see Figs. 5(b) and 4(a)), at $z/H < 0.125$, the downstream cylinders are completely shielded by the outer and inner shear layers of the upstream cylinders. From $z/H = 0.125$ to 0.5, however, the outer and inner shear layers of the upstream cylinders reattach onto the downstream cylinders. The antiphase periodic vortex shedding of the downstream cylinders occurs at $z/H > 0.125$ and the vortex shedding frequency of the downstream cylinders is about 0.167.

As our previous study of flow past four-cylinder arrays shows, a critical spacing ratio exists at the middle spanwise position: $L/D_{critical}$, where the downstream cylinders suppress vortex shedding from the upstream cylinders at this spacing ratio (Lam and Lo, 1992; Lam et al., 2003a, b). As the spacing ratio increases, the vortex shedding occurs behind the upstream cylinders. The present simulation indicates that the critical spacing ratio is around the value of $L/D = 3.5$ at $Re = 200$. Referring to Figs. 5(c) and 4(a), at $L/D = 3.5$, from $z/H = 0.25$ to 0.5; the outer shear layer of the upstream cylinder rolls up very near the downstream cylinder and the inner shear layer of the upstream cylinder reattaches at the downstream cylinder. The interference effect of wake regions from the upstream cylinders on one another is still evident at this spacing ratio. Vortex shedding occurs from both upstream and downstream cylinders at $z/H > 0.25$. At $z/H = 0.125$, the outer and inner shear layers of the upstream cylinders reattach onto the downstream cylinders. At $z/H = 0.0625$, however, the vortex shedding of the downstream cylinders is suppressed. It appears that the flow pattern around the cylinders is undergoing transition along the spanwise direction. This may lead to a change of the force and pressure characteristics, especially the fluctuating pressure characteristics.

For $L/D = 5.0$ (see Fig. 5(d)), a stronger 3-D effect is generated. From $z/H = 0.125$ to 0.5, the inner and outer shear layers of the upstream cylinders roll up into mature vortices and impinge onto the downstream cylinders. The vortex shedding frequency of the four cylinders is close to that of a single cylinder ($St = 0.192$). At $z/H = 0.0625$, the shear layers from the upstream cylinders reattach on the frontal part of the downstream cylinders. This pattern seems to resemble a necklace vortex, as mentioned in the case of the single cylinder reported by Liu et al. (2005), and implies that the flow pattern around the cylinders is undergoing a transition from the reattached flow pattern to the vortex shedding flow pattern.

Fig. 6 shows the instantaneous vorticity components [streamwise vorticity (ω_x), transverse vorticity (ω_y), and spanwise vorticity (ω_z)] of different spacing ratios at the x–z plane of the central position of cylinders 1 and 4 ($y/D = -L/(2D)$). The strength of vorticity is weakened for ω_x and ω_y compared with ω_z. Near the end wall, the wake patterns become more incoherent in the x–z plane for all the cylinder models with different spacing ratios. This may be attributed to the presence of the boundary layer with the span vortex shedding being suppressed. At $L/D = 1.6$, the vorticity in the x–z plane of the central position of cylinders 2 and 3 ($y/D = L/(2D)$) is also plotted for comparison. Because of the bistable wake pattern at such a spacing ratio, which has been shown in Fig. 5(a) (ω_x and ω_y between the four cylinders are very weak, near the middle spanwise positions, ω_x and ω_y are approximately equal to zero), while ω_z behind the downstream cylinders is much stronger and incoherent over the entire spanwise direction. From the ω_z distribution in the x–z planes at $L/D = 1.6$, a bistable shielding flow pattern can be clearly observed. Between the upstream cylinders and the downstream cylinders, no evident vorticity is generated along the spanwise direction. This also implies that the downstream cylinders are completely shielded by the shear layers from their corresponding upstream cylinders in all spanwise positions. The 3-D instability is also displayed by the ω_x, ω_y, and ω_z distributions for $L/D = 3.5$ and 5.0. At $L/D = 3.5$, ω_z shows a clearly parallel periodic vortex shedding behind the downstream cylinders. The well organized ω_z wake patterns are observed at $z/H > 2.5$. At $L/D = 5.0$, the ω_z distribution suggests that vortex shedding of small-scale spanwise wavelength with vortex dislocations occurs behind the downstream cylinders.

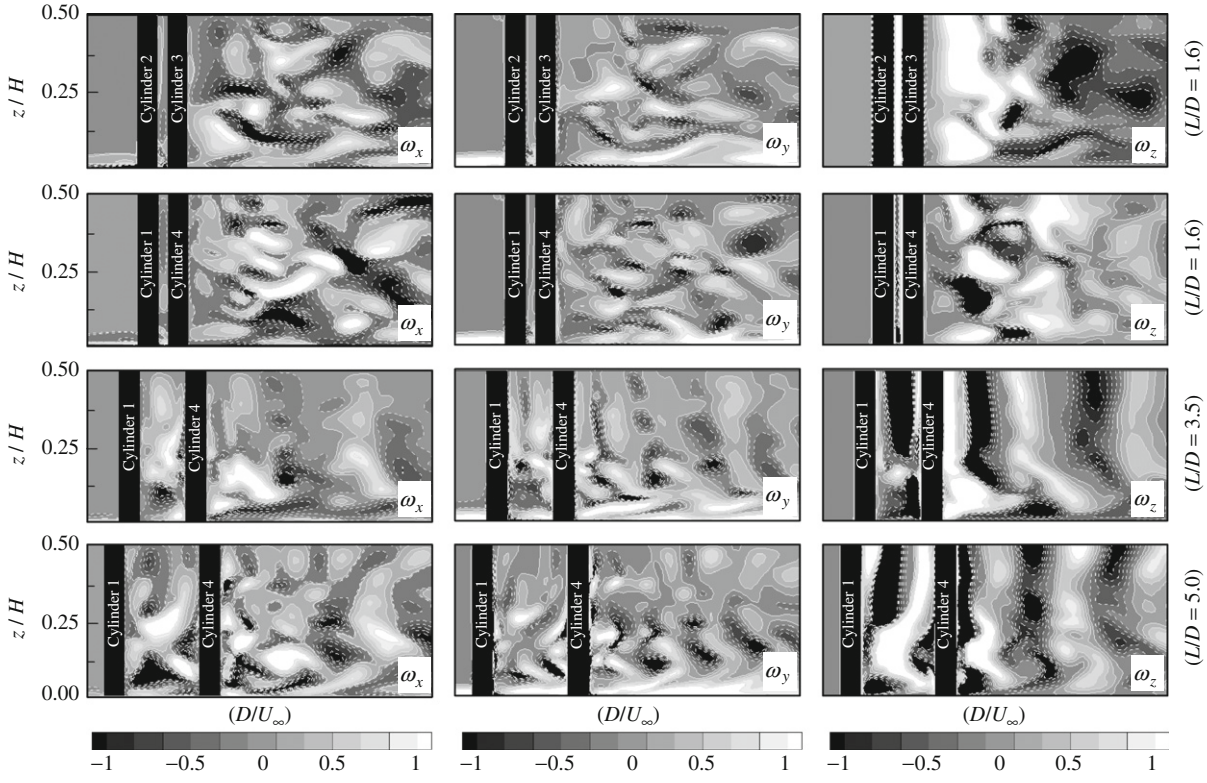

Fig. 6. Instantaneous vorticity components (ω_x, ω_y, ω_z) at different spacing ratios (L/D) in x–z plane with $H/D = 16$.

In general, due to the end wall effect, additional stronger streamwise vorticity and transverse vorticity are generated along the spanwise direction of the cylinders and tend to distort the 2-D spanwise vorticity shear layers. This kind of complex 3-D vortex structure distributions will push the free shear layers separately at further downstream positions and weaken the shear layer interaction in the near wake behind the cylinders, which will lead to reduction of drag and lift coefficients (see Figs. 5(a, b)). This also explains why the present 3-D simulation results of $\overline{C}_D$ and C'_L are smaller than the 2-D results by Lam et al. (2008). Typically for $L/D \geq 4.0$, the large discrepancies of $\overline{C}_D$ and C'_L between the 3-D and 2-D results are due to the secondary vortices generated around the mid-span positions of $z/H = 0.5$.

3.3. Effect of H/D on the 3-D vortex structures

Fig. 7 shows the instantaneous spanwise vorticity component ω_z at three different spanwise positions ($z/H = 0.0625$ (near end wall), 0.125, and 0.25) with the variation of aspect ratios ($H/D = 6$, 8, and 20) for $L/D = 3.5$ together with the case employing periodic boundary conditions at the ends of the cylinders. The 3-D vortex structures are also drawn for clearer illustration. Similar to the wake characteristics of the four cylinders with different spacing ratios, the flow patterns around the four cylinders for all aspect ratios demonstrate spanwise dependency. This flow phenomenon around the four cylinders is clearly attributed to the combined effect of aspect ratio and end conditions.

As shown in Fig. 7(a), it can be observed that for relatively short cylinders $H/D = 6$, the end wall affects the flow over the entire span and stabilizes the free shear layers so that the downstream cylinders are totally immersed in the free shear layers of the corresponding upstream cylinders, resulting in a stable shielding flow pattern over the entire span. No distinct vortex shedding can be seen behind the upstream and downstream cylinders at this aspect ratio. For $8 \leq H/D \leq 20$ (see Figs. 7(b) and (c)), however, the effects of the end wall can be found only at the part of the span near the end wall. At $z/H = 0.0625$, the stable reattachment flow pattern around the four cylinders is clearly identified and vortex shedding behind the upstream and downstream cylinders is delayed until very far downstream, because the unsteady flow is suppressed by the wall boundary layer. For $z/H \geq 0.125$, two distinct stable antiphase vortex streets about the centreline can be detected behind the downstream cylinders. Especially at $H/D = 20$, the vortices behind the

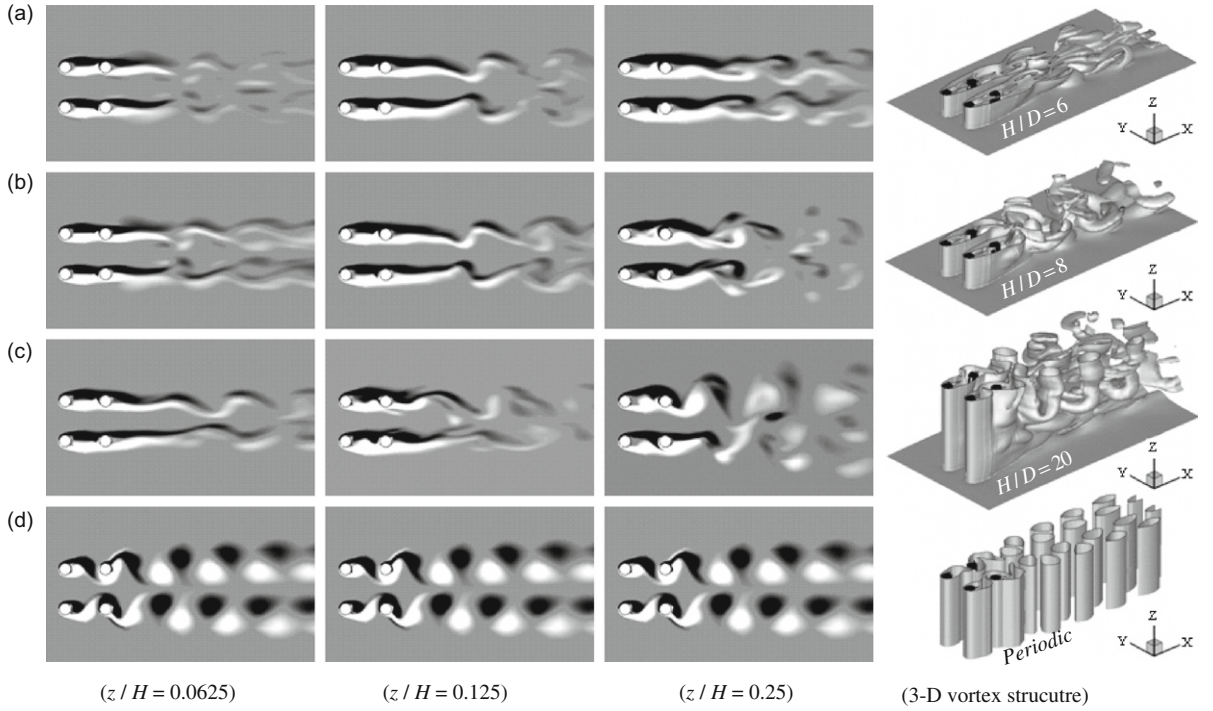

Fig. 7. Flow patterns at different spanwise positions and 3-D vortex structures for different aspect ratios compared with those that employed the periodic boundary condition at $L/D = 3.5$: (a) $H/D = 6$, (b) $H/D = 8$, (c) $H/D = 20$, and (d) periodic boundary condition.

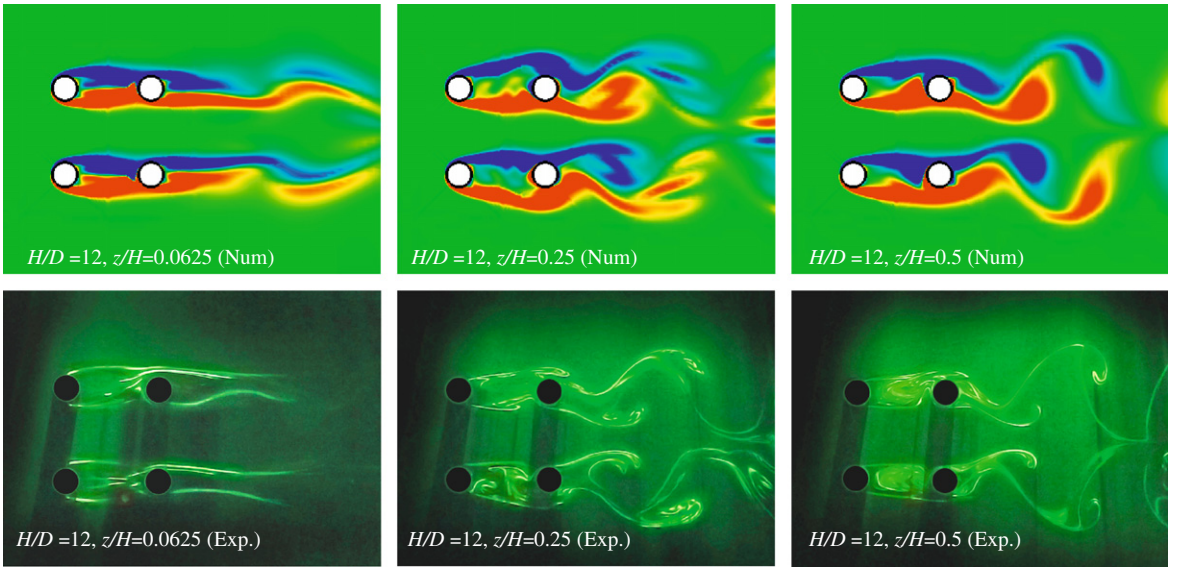

Fig. 8. Flow patterns at three different spanwise positions by numerical method and corresponding visualization results at $L/D = 3.5$ and $H/D = 12$.

downstream cylinders are fairly close to each other. They interact with each other, forming a very complex wake. Such downstream vortex interaction results in a more complex wake interference pattern around the four cylinders.

Flow visualization experiments using the LIF technique were also carried out in a low-speed closed-loop water tunnel to verify the 3-D calculated results for the case $L/D = 3.5$ and $H/D = 12$ at the same Reynolds number of 200. [For

detailed description of the water tunnel set-up and the LIF technique, please refer to Lam et al. (2003a, b).] As shown in Fig. 8, the present 3-D numerical simulation captures accurately the shielding flow pattern at the mid-span of the cylinders and predicts successfully the change of the flow pattern at different spanwise positions of the cylinders. The flow patterns are very similar to the experimental results captured by the LIF technique. This further validates the accuracy of the present numerical methods. Referring to Figs. 4(b) and 7, an unsteady shielding flow pattern around the four cylinders near the mid-span occurs over the aspect ratio range $8 \leq H/D \leq 15$, whereas the outer shear layer of the upstream cylinder begins to roll up very close to the downstream cylinder near the mid-span and exhibits a vortex reattachment flow pattern at $H/D = 16$. At $H/D = 20$, mature vortices form behind the upstream cylinder near the mid-span and then impinge on the downstream cylinder. This indicates that the flow pattern around the cylinders near the middle spanwise position undergoes a transformation from the unsteady shielding flow pattern to the vortex reattachment flow pattern, and then becomes a full vortex shedding flow pattern when the aspect ratio increases from 16 to 20. It is noted that the unsteady shielding flow pattern in the mid-span position at $H/D = 15$ is very similar to the flow behavior observed by Lam et al. (2003a) at the same aspect ratio and Reynolds numbers despite the slight difference in the spacing ratio. Such characteristics explain why the observed flow pattern in the experimental study by Lam et al. (2003a) is completely different from the 2-D simulation results by Lam et al. (2008) and Farrant et al. (2000) at the critical spacing ratio $L/D = 3.5$. This is because the aspect ratio in the experimental investigation was less than 16 and the end conditions also play an important role in the stability of the shear layer.

On the other hand, coexistence of different flow pattern over different parts of the span with the same aspect ratio is also observed. For $H/D = 20$ at $z/H \leq 0.125$, the end of the shear layer from the upstream cylinders reattaches stably on the downstream cylinders and no vortex forms behind the upstream cylinders. However, from $z/H = 0.25$ to 0.375, the vorticity distributions around the four cylinders strongly suggest that the outer shear layer of the upstream cylinders begins to roll up very near the downstream cylinders and exhibits a vortex reattachment flow pattern. At the $z/H = 0.5$, a full mature vortex shedding behind the upstream cylinders occurs. This means that the free shear layer around the cylinders undergoes a transformation from a stable reattachment flow pattern to a vortex reattachment flow pattern, and it then becomes a full vortex shedding flow pattern spanwise along the cylinders. This may be attributed to the reason that, at the higher aspect ratio, there are unsteady pressure gradients developed along the spanwise direction. These will lead to different pressure distributions along the spanwise direction. Luo et al. (1996) observed similar phenomena for finite cylinders in tandem. It is interesting to note that, for the flow pattern around four cylinders, the shear layers from the upstream cylinders roll up into mature vortices and impinge on to the downstream cylinders along the whole span of the cylinders when the periodic boundary condition is applied (see Fig. 7(d)). This again indicates that the end conditions play an important role in the stability of the free shear layer.

The wake transition dependence on aspect ratio and end conditions around the four cylinders is better illustrated by the instantaneous 3-D vorticity fields. Depending on the various aspect ratios, at the middle part along the spanwise direction, a stable shielding flow pattern is exhibited with $H/D = 6$, while an unsteady shielding flow pattern occurs at $8 \leq H/D \leq 15$. The free shear layers from the upstream cylinders begin to roll up very near the downstream cylinders at $H/D = 16$. At $H/D = 20$, shear layers from the upstream cylinders roll up into mature vorticies and impinge on the downstream cylinders. Both vortex dislocations near the wall for $8 \leq H/D \leq 20$ and second vortex dislocations at $z/H = 0.375$ for $H/D = 20$ can be clearly observed.

Fig. 9 shows the instantaneous vorticity components for different aspect ratios at the x–z plane with $y/D = -1.75$ for $L/D = 3.5$. The development of the extremely thin end-wall boundary layer and the effect of aspect ratio are captured. It can be seen that upstream cylinder 1 is subjected to a uniform flow. Vortex dislocations are observed close to the end wall, where the "no-slip" condition is applied. In general, parallel vortex shedding behind the downstream cylinders is clearly seen near the middle spanwise positions for $H/D \geq 8$. At $H/D = 6$, however, a single cell with low shedding frequency covers the entire span, showing that the end boundary conditions affect the flow over the whole span. The ω_z between cylinders 1 and 4 is very weak at $H/D = 6$ and becomes fairly strong at $H/D = 20$. This suggests that a transformation of the flow pattern occurs for different aspect ratios. The ω_x and ω_y distributions also clearly display the effect of the end wall boundary layer. At $H/D = 20$, the vortex shedding from the upstream cylinders near the middle spanwise position has strengthened the unsteady flow and hence renders the distributions of ω_x and ω_y incoherent. The 3-D instability is enhanced due to the presence of the second vortex dislocations at about $z/H = 0.375$ behind the downstream cylinders. This will lead to a different characteristic of the flow-induced forces. The time-averaged streamwise velocity distributions of cylinder arrays with different aspect ratios also present similar information (see Fig. 10). At the aspect ratio of $H/D = 6$, along the spanwise direction, the streamwise velocity recovery region behind the downstream cylinder shows evidently longer wake than that for $H/D \geq 8$, which gives rise to stable upstream free shear layers covering the downstream cylinders. Furthermore, with increasing H/D, the length of the streamwise velocity recovery region behind the upstream cylinders becomes shorter and thinner. Referring to the Strouhal number distribution (Fig. 4(b)), the vortex shedding frequency also increases at high H/D values.

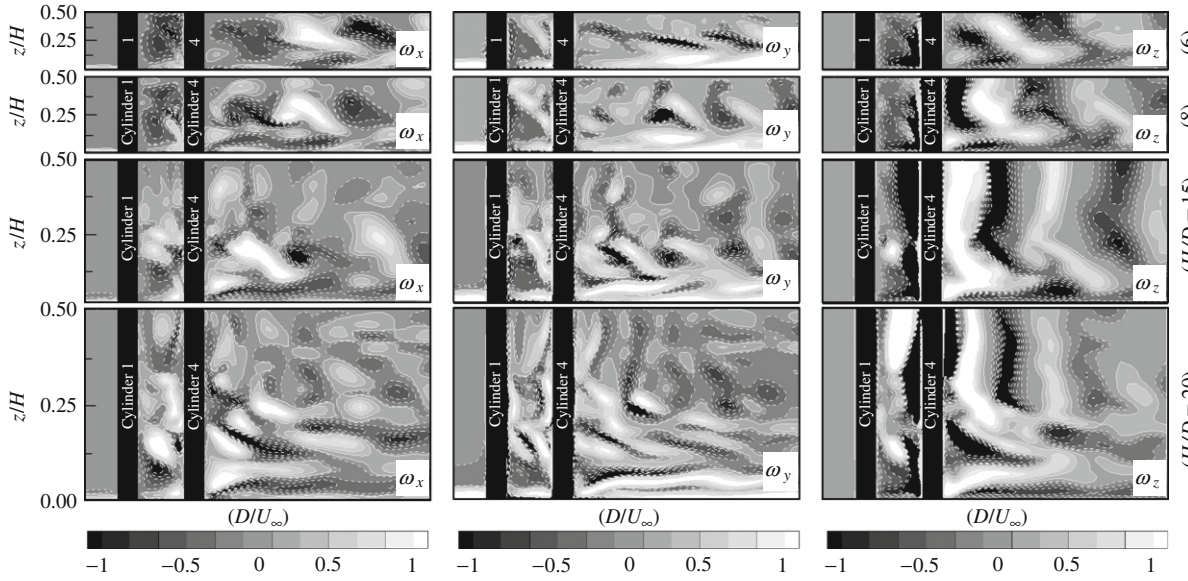

Fig. 9. Instantaneous vorticity components (ω_x, ω_y, ω_z) at different aspect ratios (H/D) in x–z plane with $L/D = 3.5$.

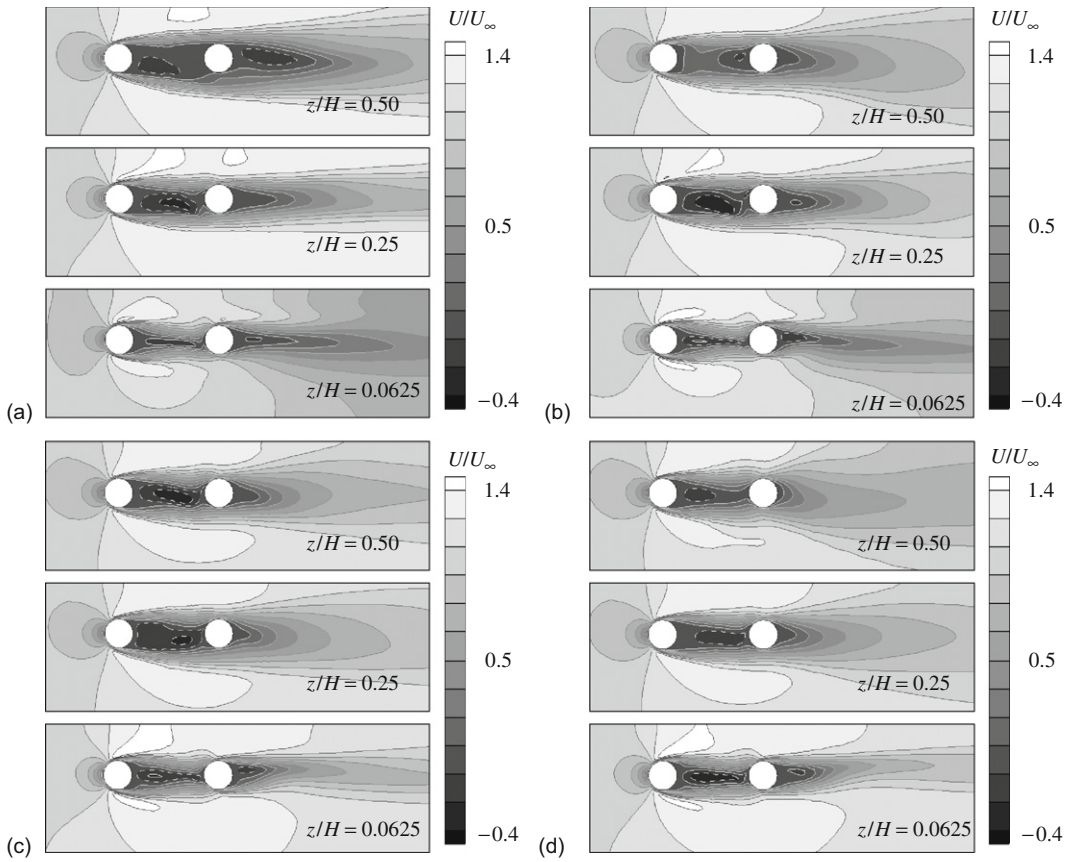

Fig. 10. Time averaged streamwise velocity distributions around cylinders 1 and 4 at different aspect ratios (H/D) in x–z plane with $L/D = 3.5$: (a) $H/D = 6$, (b) $H/D = 8$, (c) $H/D = 15$ and (d) $H/D = 20$.

The results above show that spacing ratio, aspect ratio, and end conditions have important combined effects on the flow transition mechanism around the four cylinders. In general, the flow patterns vary from a bistable shielding flow pattern to a vortex shedding flow pattern as the spacing ratio increases. Moreover, the transformation from a stable shielding flow pattern to a full vortex shedding flow pattern near the middle position along the spanwise direction of the cylinders is observed to be dependent on the aspect ratio and end conditions. Due to the highly 3-D nature of the flow, the coexistence of different flow patterns over different parts of the span at the same H/D is also displayed. Such changes of the flow patterns around the four cylinders will in turn affect the pressure distributions on the cylinders.

3.4. Effect of L/D on pressure coefficient distributions

Fig. 11 shows the mean pressure coefficient distributions of the cylinders at four different spanwise locations and different spacing ratios for aspect ratio $H/D = 16$ at $\mathrm{Re} = 200$. The pressure coefficient on the cylinder surface is defined as $C_p = (p - p_\infty)/(\frac{1}{2}\rho U_\infty^2)$, where p_∞ is the oncoming flow ambient pressure.

For upstream cylinder 1, the $\overline{C}_{p1}$ (subscripts "1" and "4" refer to the upstream cylinder 1 (CY-1) and downstream cylinder 4 (CY-4), respectively) distribution shows that the stagnation points (the positions of maximum pressure coefficients) move from the inner side ($\theta = 18^\circ$) to the frontal position ($\theta = 0^\circ$) as L/D increases from 1.6 to 5.0. This is consistent with the conclusion of Lam and Fang (1995) and Lam et al. (2008). At $L/D = 1.6$, the $\overline{C}_{p1}$ distributions are slightly asymmetric about the position of $\theta = 180^\circ$. This is due to the interaction between the inner free shear layers from upstream cylinders 1 and 2 at the small spacing ratio. The $\overline{C}_{p1}$ distribution gradually becomes symmetrical and close to that of a single cylinder when the spacing ratio L/D increases to 5.0.

For downstream cylinder 4, the $\overline{C}_{p4}$ distribution shows more distinctive changes with variation of L/D. Three types of flow patterns could be distinguished. At $L/D = 1.6$, the $\overline{C}_{p4}$ shows only one maximum and it is located at the frontal position (about $\theta = 60^\circ$) of the cylinder, suggesting reattachment points of the inner shear layer of upstream cylinder 1. The second maximum $\overline{C}_{p4}$ of downstream cylinder 4, corresponding to the reattachment point of the outer shear layer of upstream cylinder 1, does not exist for $z/H = 0.0625$–0.5. This implies that the outer shear layer from upstream cylinder 1 does not reattach to the downstream cylinder but covers the downstream cylinder 4 completely over the entire

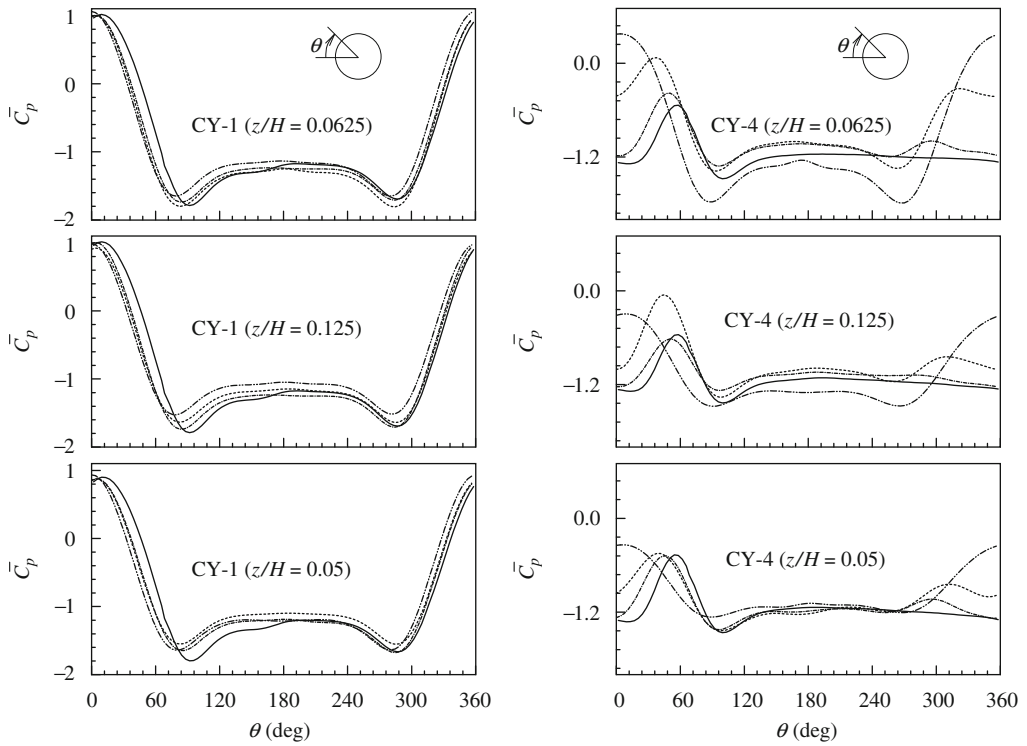

Fig. 11. Mean pressure coefficient distributions along the circumference of the four cylinders at four different spanwise positions with different spacing ratios at $H/D = 16$: ———, $L/D = 1.6$; -·-·-·-·-, $L/D = 2.5$; – – – – – – – –, $L/D = 3.5$; and -· ·-· ·-· ·-, $L/D = 5.0$.

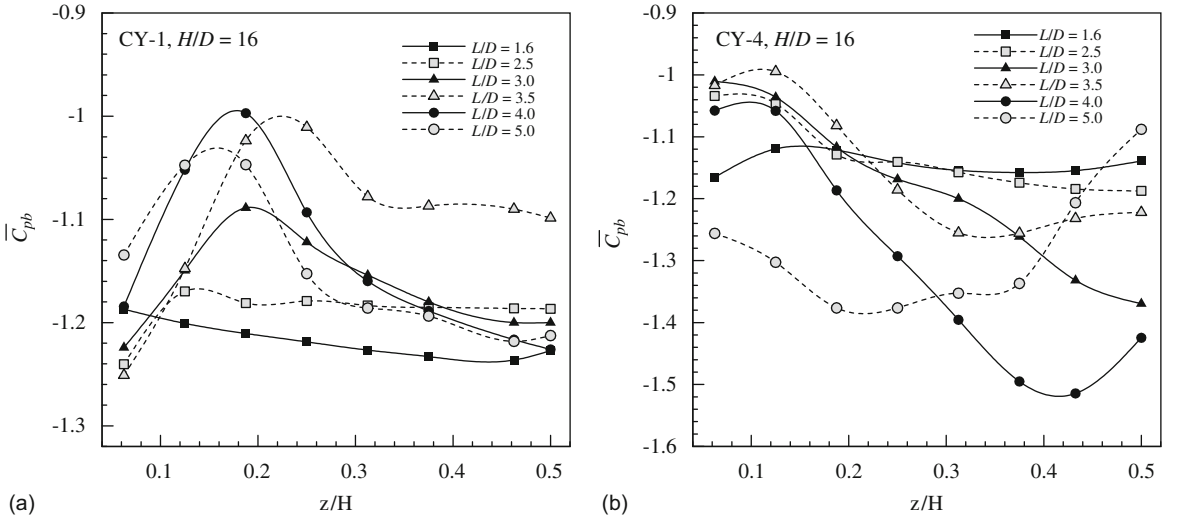

Fig. 12. Base pressure coefficients (at $\theta = 108^\circ$) on the cylinders at different spanwise positions for different spacing ratios L/D at $H/D = 16$.

span. Lam and Fang (1995) pointed out that at $L/D < 2.48$, only one maximum $\overline{C}_{p4}$ point around $\theta \approx 55^\circ$ occurs for cylinder 4. This agrees fairly well with the present results. As L/D increases to 2.5 and 3.5, two local maxima emerge. The maximum pressure points occur at $\theta \approx 50^\circ$ and 310° around the mid-span position ($z/H = 0.5$). The magnitude of the second maximum $\overline{C}_{p4}$, corresponding to the reattachment point of the outer shear layer of upstream cylinder 1, is less than the first maximum $\overline{C}_{p4}$ corresponding to the reattachment point of the inner shear layer of upstream cylinder 1. This means that the flow pattern is a reattachment flow pattern and the interference between cylinders 1 and 2 is still important. On increasing L/D further to 5.0, the maximum pressure points shift sharply to $\theta \approx 4^\circ$ and 356°, respectively. These maximum pressure points correspond to the point of impingement of vortices shed from the upstream cylinder. This also agrees with the experimental results by Lam and Fang (1995). In general, spanwise dependency can be clearly identified by the surface pressure distribution of downstream cylinder 4 when $L/D \geq 3.5$.

Fig. 12 shows the base pressure coefficient ($\overline{C}_{pb} = \overline{C}_p$ at $\theta = 180^\circ$) distributions for both the upstream and downstream cylinders at different spanwise positions. At $L/D = 1.6$ and 2.5, $\overline{C}_{pb1}$ and $\overline{C}_{pb4}$ from $z/H = 0.125$ to 0.5 are basically unchanged and show no spanwise dependency. This indicates that the effect of spacing ratio is dominant and local three-dimensionality is damped down at small spacing ratios. This behavior partially explains why the 2-D results (Lam et al., 2008) have only little discrepancy with the present 3-D results and the experimental measurements by Lam et al. (2003a) for such small spacing ratios. On increasing the spacing ratio, $\overline{C}_{pb1}$ exhibits a decreasing trend from the $z/H = 0.15$ position towards the middle spanwise position ($z/H = 0.5$) of the cylinder when $L/D \geq 3.0$. Near the end wall (from $z/H = 0.0625$ to 0.125 position), however, the trend is reversed due to the end wall effect, which has suppressed the formation of vortex shedding near the end wall. Similar phenomena have been pointed out for the flow past a single cylinder by Szepessy and Bearman (1992) and Luo et al. (1996). For downstream cylinder 4, in general, $\overline{C}_{pb4}$ decreases with increasing z/H when $L/D \geq 3.0$, while for $L/D = 4.0$ and 5.0, $\overline{C}_{pb4}$ shows an evident increasing trend for $z/H \geq 0.375$, which is different from that at other spacing ratios (see Fig. 12(b)). This may be due to the complicated secondary vortices being generated, which give rise to stronger 3-D effect on the wake vortex structures near the mid-span position ($z/H = 0.5$); refer to the flow patterns in Figs. 5(d) and 6.

To illustrate the effects of spacing ratio and end wall on the vortex shedding characteristics, which in turn have strong effects on the fluctuation pressure characteristics, the C'_p distributions are calculated and presented in Fig. 13. Along the spanwise direction, C'_p of the upstream and downstream cylinders exhibit a strong dependency on spacing ratio. The peak of C'_p has a general increasing trend towards the middle position along the spanwise direction of the cylinders at all spacing ratios. This behavior is an indication of the extent of the end wall effect on vortex shedding characteristics.

For upstream cylinder 1, the far smaller values of C'_p at $L/D = 1.6$ and 2.5 over the entire span indicate that a fairly steady free shear layer is generated. At $L/D = 3.5$, from $z/H = 0.25$ to 0.5, the values of C'_p are distinctly larger than those at $L/D = 1.6$ and 2.5. At $L/D = 5.0$, the larger pressure fluctuations indicate that the free shear layer of cylinder 1 is highly unsteady and implies that vortex shedding occurs behind the upstream cylinder. For downstream cylinder 4, the magnitude of the peak of C'_p increases significantly compared with that of the corresponding upstream cylinder.

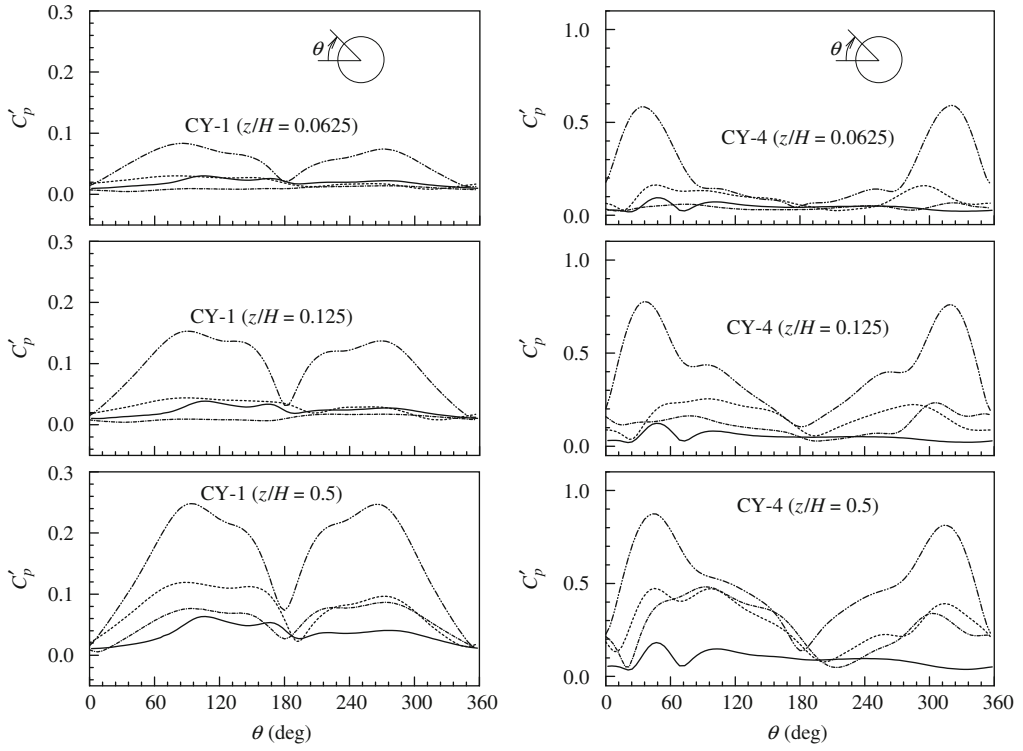

Fig. 13. Fluctuating pressure coefficient distributions along the circumference of the four cylinders at four different spanwise positions with different spacing ratios at $H/D = 16$: ———, $L/D = 1.6$; -·-·-·-, $L/D = 2.5$; – – – – – – – –, $L/D = 3.5$; and -·-·-·-·-, $L/D = 5.0$.

The relative smaller C'_p at $z/H \leq 0.125$ is attributed to the effect of the end wall except at $L/D = 5.0$. At $L/D = 1.6$, the asymmetrical C'_p implies the existence of bistable flow. At $L/D = 3.5$, the outer shear layer of the upstream cylinder rolls up very near the downstream cylinder and pushes the inner shear layer of the downstream cylinder. This enhances the instability of the inner shear layer of the downstream cylinder when $z/H \geq 0.25$. C'_p possesses two local maximum values and two local minimum values over the range $0^\circ \leq \theta \leq 180^\circ$.

3.5. Effect of H/D on pressure coefficient distributions

Fig. 14 shows the distributions of $\overline{C}_p$ and C'_p at three different spanwise positions ($z/H = 0.0625$, 0.125 and 0.5) for $H/D = 6$, 8, 14, and 16 with $L/D = 3.5$. For upstream cylinder 1, the distributions of $\overline{C}_{p1}$ in the ranges $0^\circ \leq \theta \leq 50^\circ$ and $310^\circ \leq \theta \leq 360^\circ$ are fairly insensitive to the variations of both H/D and z/H. At $80^\circ \leq \theta \leq 280^\circ$, however, aspect ratio and spanwise dependency can be clearly discerned. For the shorter cylinder model at $H/D = 6$, $\overline{C}_{p1}$ shows a strong dependency on spanwise location. $\overline{C}_{p1}$ increases continuously with increasing z/H from the position of $z/H = 0.125$ towards the middle span position ($z/H = 0.5$) of the cylinders. For $H/D \geq 8$, $\overline{C}_{p1}$ varies only slightly with z/H from a certain spanwise position towards the mid-span of the cylinder. At a certain range near the end wall, however, $\overline{C}_{p1}$ exhibits a strong spanwise dependency with an opposite trend with $H/D = 6$. The maximum effect of the end wall is detected at a distance of about $3D$ from the end wall at the aspect ratio $H/D \geq 8$. As discussed in relation to Fig. 7, the necklace type vortices behind the upstream cylinders near the end wall considerably influence the rear surface pressure and create a local maximum pressure distribution at a distance of about $3D$ from the end wall along the span. The phenomenon shows that there is a significant unsteady 3-D flow around the four cylinders close to this plane for $H/D \geq 8$.

It can be seen that the $\overline{C}_p$ distributions of downstream cylinder 4 show distinct aspect ratio and spanwise position dependency. At $z/H \leq 0.125$, two maximum pressure peaks can be observed for all aspect ratios. This implies that the reattachment of the inner and outer free shear layers from upstream cylinder 1 occurs due to the effect of the end wall and produce similar flow characteristic for all aspect ratios. This flow characteristic is supported by the vortex

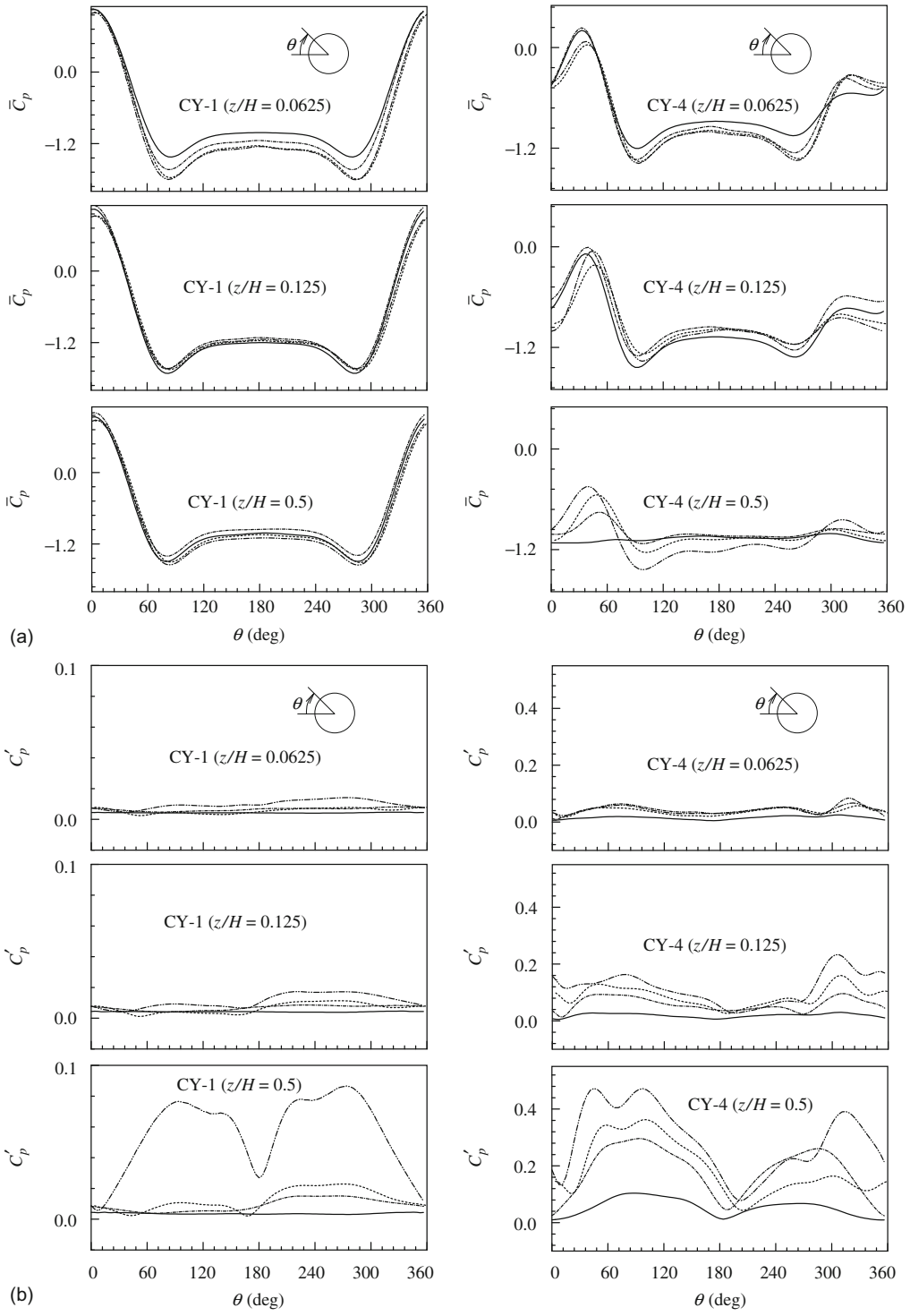

Fig. 14. Mean pressure coefficient (a) and fluctuating pressure coefficient (b) distributions along the circumference of the four cylinders at four different spanwise positions with different aspect ratios at $L/D = 3.5$ compared with those that employed the periodic boundary condition (c): ———, $H/D = 6$; -·-·-·-·-, $H/D = 8$; ¯¯¯¯¯¯¯¯, $H/D = 14$; -·· ·-·· ·-·· ·-, $H/D = 16$; and ¯¯¯¯¯, periodic boundary condition.

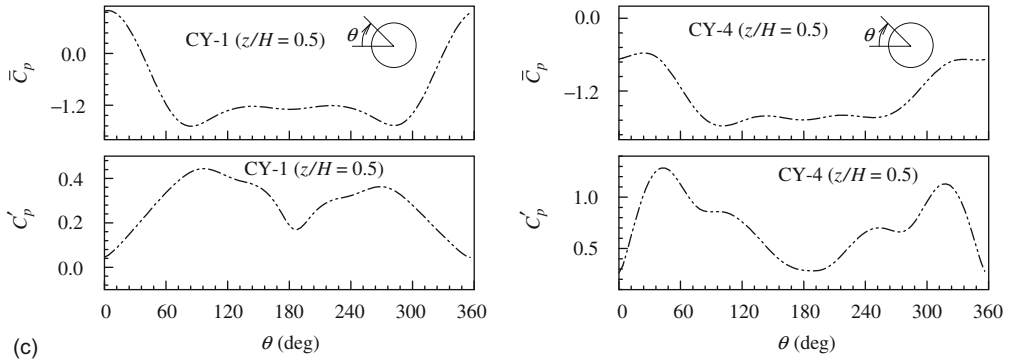

Fig. 14. (*Continued*)

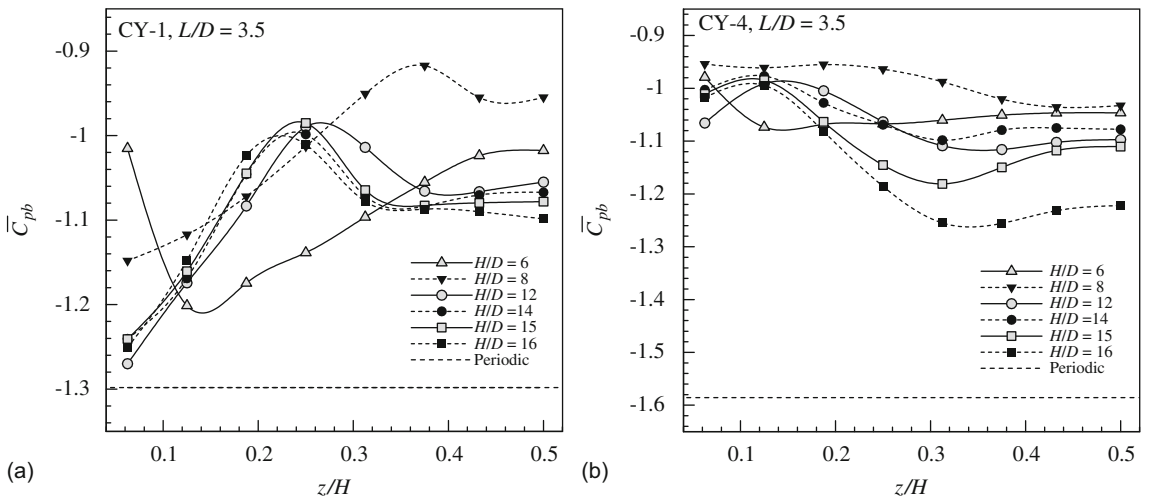

Fig. 15. Base pressure coefficients (at $\theta = 180^\circ$) on the cylinders at different spanwise positions for different aspect ratios H/D at $L/D = 3.5$.

structures at $z/H = 0.0625$ (see Fig. 7). Three types of flow pattern can be distinguished based on the $\overline{C}_{p4}$ for $z/H > 0.25$. At $H/D = 6$, $\overline{C}_{p4}$ drifts continuously to the negative territory as z/H increases, while it becomes flat at $z/H = 0.5$. No reattachment position can be detected. Such $\overline{C}_{p4}$ characteristics suggest a complete stable shielding flow pattern around the four cylinders with no vortex dislocation occurring. For $8 \le H/D \le 14$, there is only one distinct maximum point in the range $0^\circ \le \theta \le 100^\circ$ and $0.25 \le z/H \le 0.5$. The $\overline{C}_{p4}$ characteristic implies that the inner free shear layer from the upstream cylinders become unstable and an unsteady shielding flow pattern has developed. At $H/D \ge 15$, two maximum pressure peaks with obvious distinction are found. The $\overline{C}_{p4}$ from $z/H = 0.25$ to 0.5 suggests that the free shear layers from upstream cylinder 1 roll up very near downstream cylinder 4 and hence a vortex reattachment flow pattern is generated.

The same characteristic discussed regarding Fig. 14 can also be observed in Fig. 15 for $\overline{C}_{pb}$ of the cylinder arrays with different H/D and z/H. A local maximum of $\overline{C}_{pb}$ along the spanwise direction for the upstream cylinder 1 occurs at a distance of approximately $3D$ from the end wall. As for downstream cylinder 4, due to the effect of the end conditions, it occurs at a distance of approximately $2D$ from the end wall (except for the short cylinder case of $H/D = 6$, which displays an opposite characteristic). At the middle spanwise position, the $\overline{C}_{pb}$ of the upstream and downstream cylinders reduces as H/D increases except at $H/D = 6$. There is a large drop of the base pressure of downstream cylinder 4 from $H/D = 15$ to 16. This again signifies that a transformation of flow pattern has occurred.

Fig. 14(b) shows the distributions of fluctuation pressure C'_p with aspect ratio for cylinders 1 and 4 at $L/D = 3.5$. In general, the peak of C'_p has an increasing trend towards the middle spanwise position of the cylinders for all aspect

ratios. At $0.0625 \le z/H \le 0.125$, the C'_p of the upstream and downstream cylinders is very low at all aspect ratios due to the free shear layers being stabilized by the effect of the end wall. At $H/D = 6$, very small C'_p with little variation is found around all cylinders over the entire span position. This indicates that a stable shielding flow pattern occurs throughout the entire span. For $H/D \ge 8$, however, the C'_p of the upstream and downstream cylinders exhibits a strong aspect ratio dependency for $0.25 \le z/H \le 0.5$. All the characteristics are quite different from the characteristics shown in Fig. 14(c), where periodic boundary conditions have been employed.

For upstream cylinders, at $8 \le H/D \le 14$, a slightly lower fluctuation pressure coefficient distribution C'_{p1} is observed over the range $0^\circ \le \theta \le 180^\circ$ than that over the range $180^\circ \le \theta \le 360^\circ$ along the entire span. This suggests that the interference between the wake of upstream cylinders 1 and 2 exists. The outer free shear layer of the upstream cylinder becomes unsteady. When H/D increases to 16, the maximum C'_{p1} increases sharply up to approximately 4 times the others. This is attributed to the transformation from a shielding flow pattern to a vortex reattachment flow pattern. The C'_{p1} displays a distinct jump from $z/H = 0.125$ to 0.5. This indicates that a flow pattern transformation at $H/D \ge 8$ along the spanwise direction occurs. For downstream cylinder 4, the peak of the C'_{p4} is significantly larger than that of the corresponding upstream cylinder 1. This is attributed to the reason that higher vortex shedding strength will lead to higher pressure fluctuations. At $z/H = 0.125$, C'_{p4} fluctuates up and down rapidly with a smaller amplitude over the range $180^\circ \le \theta \le 360^\circ$. This is due to the unsteady outer free shear layer of the downstream cylinder interacting with the vortex dislocations near the end wall. Compared with the case of the cylinder array with periodic boundary conditions, C'_p is much smaller for the cylinder array with end wall boundary conditions (see Figs. 14(b) and (c)). This is consistent with the force coefficient results in Figs. 3(c) and (d).

4. Conclusions

This paper presents a 3-D numerical investigation of the effects of spacing ratio, aspect ratio, and no-slip end wall conditions on laminar flow around four circular cylinders in in-line square configurations at a Reynolds number of 200. Experimental measurements were also carried out for the validation of the numerical study. The numerical results are in good agreement with the experimental results. Instantaneous 3-D flow patterns and other quantitative information were obtained. Such information is very helpful for better understanding the complex flow characteristics around the cylinder array. The major results are summarized as follows.

In general, the wake pattern varies from a bistable shielding flow pattern ($L/D = 1.6$) to a vortex shedding flow pattern ($L/D = 5$) with an increase of the spacing ratio. The critical spacing ratio at this Reynolds number is around the value $L/D = 3.5$ for all the aspect ratios studied. Due to the highly 3-D nature of the flow generated along the spanwise direction resulting from effect of end-wall conditions, the fluctuating pressure coefficient distributions of both upstream and downstream cylinders exhibit a strong spanwise dependency. The transformation of the flow pattern has a great effect on the mean pressure coefficient distributions over the downstream cylinders, but has only a little effect on that of the upstream cylinders.

The aspect ratio together with the end wall conditions have prominent combined effects on the distribution of both the mean pressure coefficients and the fluctuating lift coefficients for the four cylinders along the spanwise direction. All the downstream cylinders show strong aspect ratio and spanwise dependency. The changes of the drag and fluctuating lift coefficients on the downstream cylinders are significantly larger than changes on the upstream cylinders for all aspect ratios. The aspect ratio and end conditions have important combined effects on the transition mechanism of flow patterns around the four cylinders. Transformation of flow pattern from a stable shielding flow pattern to a full vortex shedding flow pattern near the middle spanwise positions of the cylinders was observed with an increase of aspect ratio. Such a transformation of flow pattern along the span has a strong effect on the mean pressure coefficient distributions of the downstream cylinders, but only a small effect on the upstream cylinders. The maximum effect of the end wall was found to be at a distance of approximately $3D$ from the end wall for aspect ratio $H/D \ge 8$. The "necklace" type vortices behind the upstream cylinders near the end wall had considerable influence on the rear surface pressure along the spanwise locations and led to a local maximum base pressure at a distance of approximately $3D$ from the end wall. The developments of free shear layers, mean and fluctuating pressure coefficients as well as force coefficients are critically affected by the cylinder aspect ratio in the range $H/D = 15$–16.

Due to the highly 3-D nature of the flows, the coexistence of different flow patterns over different spanwise locations was observed for all the present cylinder models with different spacing and aspect ratios. The results are all quite different from those obtained with periodic boundary conditions at the cylinder ends for infinitely long cylinders and the results of 2-D simulations. We conclude that 2-D simulations are not generally sufficient to reveal the complex flow characteristics for flow around four cylinders in an in-line square configuration.

Acknowledgements

The authors wish to thank the Research Grants Council of the Hong Kong Special Administrative Region, China, for its support through Grant no. PolyU 5299/03E.

References

Carmo, B.S., Meneghini, J.R., 2006. Numerical investigation of the flow around two circular cylinders in tandem. Journal of Fluids and Structures 22, 979–988.

Chan, C.T., Anastasiou, K., 1999. Solution of incompressible flows with or without a free surface using the finite volume method on unstructured triangular meshes. International Journal on Numerical Methods in Fluids 29, 35–57.

Farrant, T., Tan, M., Price, W.G., 2000. A cell boundary element method applied to laminar vortex-shedding from arrays of cylinders in various arrangements. Journal of Fluids and Structures 14, 375–402.

Fey, U., König, M., Eckelmann, H., 1998. A new Strouhal–Reynolds number relationship for the circular cylinder in the range $47 < \mathrm{Re} < 2 \times 10^5$. Physics of Fluids 10 (7), 1547–1549.

Kevlahan, N.K.-R., 2007. Three-dimensional Floquet stability analysis of the wake in cylinder arrays. Journal of Fluid Mechanics 592, 79–88.

Lam, K., Cheung, W.C., 1988. Phenomena of vortex shedding and flow interference of three cylinders in different equilateral arrangements. Journal of Fluid Mechanics 196, 1–26.

Lam, K., Lo, S.C., 1992. A visualization study of cross-flow around four cylinders in a square configuration. Journal of Fluids and Structures 6, 109–131.

Lam, K., Fang, X., 1995. The effect of interference of four equispaced cylinders in cross flow on pressure and force coefficients. Journal of Fluids and Structures 9, 195–214.

Lam, K., Li, J.Y., Chan, K.T., So, R.M.C., 2003a. Flow pattern and velocity field distribution of cross-flow around four cylinders in a square configuration at low Reynolds number. Journal of Fluids and Structures 17, 579–665.

Lam, K., Li, J.Y., So, R.M.C., 2003b. Force coefficient and Strouhal numbers of four cylinders in cross flow. Journal of Fluids and Structures 18, 305–324.

Lam, K., Zou, L., 2007. Experimental and numerical study for the cross-flow around four cylinders in an in-line square configuration. Journal of Mechanical Science and Technology 21, 1338–1343.

Lam, K., Gong, W.Q., So, R.M.C., 2008. Numerical simulation of cross-flow around four cylinders in an in-line square configuration. Journal of Fluids and Structures 24, 34–57.

Liu, Y., So, R.M.C., Cui, Z.X., 2005. A finite cantilevered cylinder in a cross-flow. Journal of Fluids and Structures 20, 589–609.

Luo, S.C., Gan, T.L., Chew, Y.T., 1996. Uniform flow past one (or two in tandem) finite length circular cylinder(s). Journal of Wind Engineering and Industrial Aerodynamics 59, 69–93.

Mittal, S., 2001. Computation of three-dimensional flows past circular cylinder of low aspect ratio. Physics of Fluids 13, 177–191.

Moulinec, C., Hunt, J.C.R., Nieuwstadt, F.T.M., 2004. Disappearing wakes and dispersion in numerically simulated flows through tube bundles. Flow, Turbulence and Combustion 73, 95–116.

Norberg, C., 1994. An experimental investigation of the flow around a circular cylinder: influence of aspect ratio. Journal of Fluid Mechanics 258, 287–316.

Norberg, C., 2003. Fluctuating lift on a circular cylinder: review and new measurements. Journal of Fluids and Structures 17, 57–96.

Okamoto, S., Sunabashiri, Y., 1992. Vortex shedding from a circular cylinder of finite length placed on a ground plane. Transactions of the ASME: Journal of Fluids Engineering 114, 512–527.

Persillon, H., Braza, M., 1998. Physical analysis of the transition to turbulence in the wake of a circular cylinder by three-dimensional Navier–Stokes simulation. Journal of Fluid Mechanics 356, 23–88.

Sayers, A.T., 1988. Flow interference between four equispaced cylinders when subjected to a cross flow. Journal of Wind Engineering and Industrial Aerodynamics 31, 9–28.

Sayers, A.T., 1990. Vortex shedding from groups of three and four equispaced cylinders situated in cross-flow. Journal of Wind Engineering and Industrial Aerodynamics 34, 213–221.

So, R.M.C., Liu, Y., Cui, Z.X., Zhang, C.H., Wang, X.Q., 2005. Three-dimensional wake effects on the flow-induced forces. Journal of Fluids and Structures 20, 373–402.

Szepessy, S., Bearman, P.W., 1992. Aspect ratio ad end plate effects on vortex shedding from a circular cylinder. Journal of Fluid Mechanics 234, 191–217.

Williamson, C.H.K., 1996. Three-dimensional wake transition. Journal of Fluid Mechanics 328, 345–407.

Zhang, J., Dalton, C., 1998. A three-dimensional simulation of a steady approach: past a circular cylinder at low Reynolds number. International Journal of Numerical Methods in Fluids 26, 1003–1022.